Mesoscopic Effects in Ferromagnetic Materials

A Dissertation
Presented to
The Academic Faculty

by

Xiya Liu

In Partial Fulfillment
of the Requirements for the Degree
Doctor of Philosophy
in
School of Physics

School of Physics
Georgia Institute of Technology
August 2008

Mesoscopic Effects in Ferromagnetic Materials

Approved by:

Dr. Dragomir Davidovic, Advisor
School of Physics
Georgia Institute of Technology

Dr. Markus Kindermann
School of Physics
Georgia Institute of Technology

Dr. Alexei Marchenkov
School of Physics
Georgia Institute of Technology

Dr. David Citrin
School of Electrical and Computer Engineering
Georgia Institute of Technology

Dr. Elisa Riedo
School of physics
Georgia Institute of Technology

Date Approved: April 24, 2008

To my parents

ACKNOWLEDGEMENTS

I would like to take this opportunity to express my gratitude to many people. First of all, I want to thank my advisor Dr. Dragomir Davidovic, for his guidance, support and encouragement over the years. This thesis would not have been possible without him. I also want to thank my committee members Dr. Alexei Marchenkov, Dr. Elisa Riedo, Dr. Markus Kindermann and Dr. David Citrin for their expertise and advice. Special thanks go to Dr. Yaguang Wei, Dr. Liyuan Zhang, Chris Malec, Felipe Birk and former group members for being so nice people to work with. Finally, I would like to thank my parents for their endless love.

TABLE OF CONTENTS

LIST OF FIGURES

SUMMARY

The understanding of the transport properties of condensed matter system has advanced dramatically in the past decades. Concepts such as weak localization, electron-electron interaction enhancement effect and conductance fluctuations have been developed. This progress gains high interests from a wide range of areas, because our ability has increased significantly to fabricate micron scale samples from a variety of materials. In micron scale metallic samples at low temperatures, interference among scattered electron waves creates noticeable contributions to sample resistance. One remarkable consequence is that the resistance of phase-coherent samples becomes sensitive to the magnetic field applied on and the microscopic changes of impurity positions.

In this dissertation we present our experimental discoveries on mesoscopic electron transport in ferromagnetic materials, with a particular focus on the resistance of mesoscopic ferromagnets at low temperatures, and its sensitivity to the magnetic state of the conductor sample. We demonstrate the first observation of significant wave-function phase shifts induced by the magnetization-reversal process in Cobalt Nanoparticles. The phase shift is not caused by the Aharonov-Bohm effect, but is explained by the mistracking effect, where electron spins lag in orientation with respect to the moments inside domain walls. The dephasing length of our Co nanoparticles at low temperatures is only 30nm, much shorter than that in normal metals. Short dephasing length is correlated with the magnetocrystalline anisotropy. The experimental measurements are presented on mesoscopic resistance fluctuations and we study how the fluctuations respond to magnetization-reversal process with bias voltage and bias fingerprints. We also study quantum transport in NiFe nanoparticles, and find unforeseen phenomena which are quite different from those in Cobalt. By these experiments, mesoscopic ferromagnetism provides information not accessible by classical MR techniques, although the interpretation of phase coherent phenomena in ferromagnets remains a challenge, It is a promising technique for deepening our understanding of the

coupling between conduction electrons and magnetic moments in ferromagnets.

CHAPTER I

INTRODUCTION

Mesoscopic effects have been well established in normal metals [1, 2, 3]. However, the mesoscopic effects in ferromagnetic materials are not studied in detail and are different from those in normal metals. Normal metals with a short mean free path do not exhibit magnetoresistance (MR) at high temperatures. By contrast, weakly disordered ferromagnets with a similar mean free path exhibit MR. Therefore, MR has been an active research topic on ferromagnets for decades. It has been recently found that MR could lead to novel mesoscopic effects, such as mesoscopic anisotropic magnetoresistance [4]. In this dissertation, we present our experimental discoveries on the mesoscopic electron transport in ferromagnetic materials.

As a starting point of our work on the mesoscopic effects in ferromagnets, we study the MR in ferromagnets. Magnetoresistance generally includes three different types: (i) Anisotropic magneto-resistance (AMR), which is originated from the s-d bands scattering. The sample resistance changes as the angle between magnetization and current changes. (ii) Domain wall resistance (DWR),which is caused by the interaction between conduction electrons spins and magnetization spins. Domain wall is the transition region between two differently oriented magnetic domains, the wall thickness is between 1 nm and 200 nm in most cases. (iii) Giant magnetoresistance (GMR), which is present in sandwich shaped systems with a layer of normal metal between two layers of ferromagnets. Since our samples have only one layer of ferromagnets, GMR is not present. So we discuss only AMR and DWR.

The electrical resistance of ferromagnetic materials can be represented by a phenomenological relation in which there is a field independent part and the part which depends on the angle between the direction of electrical current and orientation of magnetic field. This so-called AMR is caused by band-structure effects. The spin-orbit interaction causes the

d-bands to depend on the angle angle between current and magnetization. So, the interband scattering rate (sd) depends on direction of electron velocity. Although AMR effect is weak, electron wave-vectors at the Fermi level may change sufficiently to cause a mesoscopic AMR [4].

The AMR theory accounts well for the MR observed in bulk materials, where a very slow change of magnetization is assumed and hence the conduction electrons feel only the average magnetization. However, this assumption may not be good in magnets which contain many domains with different directions of the local magnetization. The boundary between these domains is called "domain wall", which exits in multi-domain magnets. As the conduction electrons passing through a domain wall, their spins rotate spatially within a small distance. Such domain walls would lead to the scattering of conduction electrons, which is not taken into account in the standard AMR argument. In addition, the dipolar field within the domain wall gives rise to a separate contribution to AMR. The DWR would then appear in the MR as discrete jumps in resistance versus magnetic field [5]. As for electron transport devices, the DWR can be interpreted as the result of weakly unparallel transport because of the generation of effective potential barrier. In most ferromagnets, domain wall can have a substantial effect on resistivity.

The MR can be observed at high and low temperatures if certain requirements are met. It can be analyzed together with the classical transport theory in order to calculate the total resistance for metallic materials at high temperature. However it is far from enough for micron scale metallic samples at low temperature, in which quantum corrections need to be taken into account in addition to the classical transport. Quantum corrections to resistance are significant due to correlation-induced degrees of freedom not present in normal metals (e.g., spin waves), and the interplay of ferromagnetic order with coherence. The major effects in this scenario include weak localization effect (WL), Conductance fluctuations(CF), and Electron-electron interaction enhancement effect(EE).

In mesoscopic regime, many new concepts and phenomena emerge. Weak localization, a phenomenon that conductance is suppressed by the interference [6], can be described in terms of an amplitude of two electrons propagating in opposite directions interfering with

each other after multiple impurity scatterings. The amplitudes of forward and backward scattering are leading to an enhanced probability of return. Both weak localization and electron-electron interaction could contribute significantly to the temperature dependence of the low-temperature sheet resistance in two-dimensional (2D)films [7]. In three-dimensional (3D) samples, the temperature dependence of the low-temperature resistivity in the absence of a magnetic field arises mainly from the EE.

Experimental studies have revealed unexpected fluctuations of resistance as a function of magnetic field (CF) as well [6, 8, 9]. The conductance fluctuations are not noise in the usual sense, i.e., random, time-dependent changes in the resistance, but are time-independent stochastic MR patterns which vary between samples but are reproducible at given temperature within a given sample. Theoretical investigations of these phenomena have made people to believe that conductance fluctuations are indeed a quantum interference effect. Rather interestingly, even if the background conductances differ over several orders of magnnitude, the conductance fluctuations have a universal amplitude in mesoscopic scale samples belonging to the weak localization regime. The amplitude decreases slowly with increasing temperature for a sample of fixed size, or slowly with increasing size of the sample at a fixed, nonzero temperature.

Another remarkable consequence of quantum interference is that the resistance of phase-coherent samples becomes sensitive to microscopic impurity configurations. Signatures of mesoscopic electron transport in ferromagnets have been reported in detail [10, 11, 12, 13]. However, the dependence of the wave-function interference on magnetization-reversal processes have not been measured yet.

In this work we focus our investigations on the resistance of mesoscopic ferromagnets at low temperatures and find a similar result, that the resistance is very sensitive to the magnetic state of the sample. Just like mesoscopic samples are sensitive to microscopic impurity configuration, they are sensitive to the microscopic changes in the magnetization of the ferromagnet. In particular, we observe significant wave-function phase shifts generated by domain walls. We demonstrate mesoscopic resistance fluctuations induced by the magnetization-reversal process in a cobalt nanoparticle, and study how the fluctuations

with bias voltage, bias fingerprints, respond to magnetization-reversal processes. Bias fingerprints rearrange when domains are nucleated or annihilated. The domain wall causes an electron wave function-phase shift of $\approx 5\pi$. We explain how it arises from the mistracking effect, where electron spins lag in orientation with respect to the moments inside the domain wall. Dephasing time in cobalt at 0.03 K is short, $\tau_\phi \approx 1$ ps, which we attribute to the strong magnetocrystalline anisotropy.

This dissertation innovatively introduces one of the first direct measurements of quantum interference effect induced by magnetic reversal. Mesoscopic ferromagnetism in our experiments provides information not accessible by classical MR techniques. This information is hard to interpret, but it is a promising technique for research in nanomagnetism.

CHAPTER II

THEORETICAL BACKGROUND

To study and understand the mesoscopic effects in ferromagnetic materials, we need to understand the physics lying under mesoscopic transport phenomena. Therefore, we start with as broad a base as possible with the basics of ferromagnetic materials and its coupling to the electron transport system. Then the magnetoresistance effects are discussed in normal metals and ferromagnets. Finally we narrow in to specific magnetic and electron transport effects which are related to the particular effects we have observed in the experiments.

2.1 Ferromagnetic System

Ferromagnetic materials are magnetic materials that exhibit two distinct characteristics: spontaneous magnetization and the existence of magnetic ordering temperature. The spontaneous magnetization is the net magnetization that exists inside a uniformly magnetized microscopic volume in the absence of external magnetic field. The magnitude of this magnetization is dependent on the spin magnetic moments of electrons. The electronic exchange forces in ferromagnetic materials are very large. At the Curie temperature (T_C), the thermal energy eventually overcomes the exchange energy and produces a randomizing effect such that ferromagnetic materials become paramagnetic materials at temperatures above T_C.

The common ferromagnetic materials include Cobalt, Iron, Nickel, Dysprosium, Gadolinium, and Yttrium iron garnet. The materials are widely used in a variety of applications, such as permanent magnets, electrical motors, magnetic memories, power generation and inductors. Hence, the research on ferromagnetic materials has been active and remained as hot topics for decades. Since more than a century ago, numbers of studies [14, 15] have been carried out on the electric transport properties in ferromagnetic metals. They revealed many remarkable features which are not seen in non-magnetic metals.

2.1.1 Ferromagnets

Magnetic ordering rises from the interactions between the magnetic moments of the individual atoms. This interaction can favor parallel or antiparallel alignment of the moments. In ferromagnetic materials, the moments tend to align. The alignment fights with thermal excitations that try to randomize the orientations of the spins. As mentioned above, thermal excitations overpower alignment at the Curie temperature T_C. The principle of ferromagnetism can be understood from some basic measured properties.

One of the most common ferromagnetic materials is Fe. At room temperature, the saturation magnetization of Fe is on the order of a Tesla. However, with the application of an external magnetic field at room temperature, direction of magnetization can be controlled. Moreover, Fe shows hysteresis: the magnetization is dependent on what magnetic field has most recently been applied and can be reset over and over again. Interactions between the atomic magnetic moments result in this anomalous behavior. In short range, there is a powerful exchange force which operates between one particular atom and its nearest neighbors. The exchange interaction, in general, arises from a competition of Coulomb repulsion and Fermi statistics [16]. In long range, the magnetic moments interact as dipoles over distances much longer than the atomic spacing. Though the dipole interaction falls, it can become large for large collections of atoms [17].

The competition between these two forces drives to the formation of magnetic domains. Domains are defined for the regions in which all of the magnetic moments point in the same direction, yielding to the short range exchange force. Different domains are separated by domain walls, a relatively small region in which transitions from one domains magnetization to another. Domain walls are generally the manifestation of the energy cost of the long range force. Pierre Weiss first proposed, in 1930, the presence of domains and domain walls [16].

The size of the exchange coupling will differentiate the system in different ways to minimize its energy. Two extreme cases are shown in Figure 2.1: Large Exchange Coupling (Figure 2.1A) and Small Exchange Coupling (Figure 2.1B). The large exchange coupling makes interfaces of opposite moments very unfavorable. The sample is assumed to be small enough such that the energy required to create the magnetic induction outside the

sample is less than the energy required to create a domain wall to partition a single domain. In a different case, the small exchange coupling costs relatively little energy to form the interfaces of anti-parallel moments necessary to create a domain wall. Sufficient domains are then created to allow closed loops of magnetic induction in the sample.

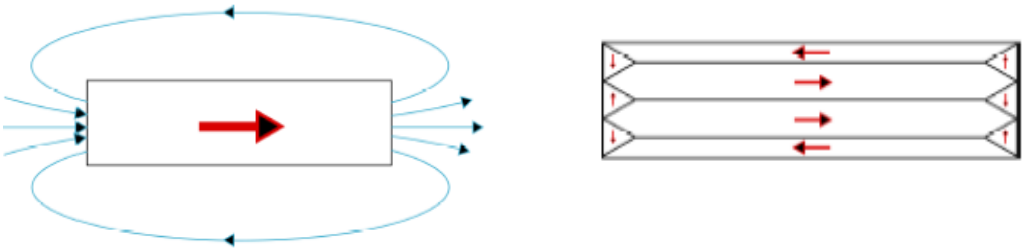

(a) Single-domain encompasses (b) Multiple-domain encompasses

Figure 2.1: (a) - A single domain encompasses an entire sample, the magnetization M represented in red. There are necessarily large compensating external fields He shown in blue. (b) - The sample is split up into many domains, magnetization in red [24]

An externally applied magnetic field can change the domain configurations of ferromagnetic materials rather than actually add energy into the changing local moments. The magnetization of such a material depends critically on what has been done to its domains over recent history. In other words, because of their domain dynamics, ferromagnetic materials exhibit hysteresis.

The general form of the magnetization hysteresis loop for a ferromagnet is shown in figure 2.2. When manipulated by an external field H_e, the magnetization M behaves as follows: from zero magnetization, M increases along the initialization curve up to the saturation magnetization M_s as the external magnetic field H_e increased to H_s. Then M decreases from M_s to the remnant magnetization M_r, as H_e is reduced to zero. M will not come back to zero until H_e is increased in the opposite direction to $-H_c$, where H_c is called the coercive field. Continually increase H_e in the opposite direction to $-H_s$, M will be saturated again, but in the opposite direction. Now, if H_e is changed from $-H_s$ to H_s, M will following the loop in figure 2.2. There are large differences between the hysteresis loops of different materials. For many soft magnetic materials, H_c is of the order of 1 A/m, but for hard magnetic materials, H_c is above 10^4 A/m generally. Practically, this wide range

provides the flexibility of different industrial usage.

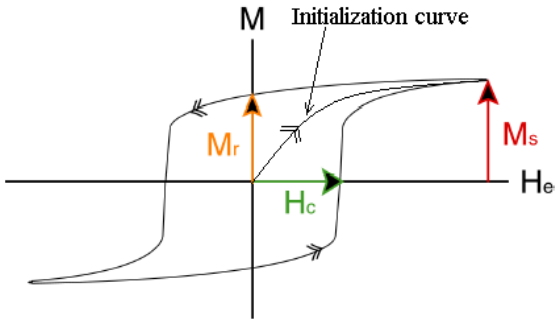

Figure 2.2: A characteristic hysteresis loop for a ferromagnet. The coercive field H_c, saturation magnetization M_S, and remnant magnetization M_r are labeled[24]

2.1.2 Electron Transport Model

In this section we introduce some important models of electron transport through materials. The electron transport depends on the shape of the sample, the disorder in the material, and the Fermi energy. We begin with the classical electron transport model through materials. Then the simplified band structure *sd* model pertinent to ferromagnetic materials is described. Although there are other recent developed models, such as the two-resistor model for spin-dependent transport, we will cover those in the later sections that discuss anisotropic magnetoresistance effect and domain wall resistance.

2.1.2.1 Classical Electron Transport Model

In classical considerations, conduction electrons are treated as an ideal gas. it is assumed that between collisions, the electron-electron interactions and electron-ion interactions are ignorable, and only the elastic collisions between electrons and impenetrable ion cores happen. Besides, the probability of an electron encountering a collision in an infinitesimal time interval dt is dt/τ, where τ is the so called mean free time or relaxation time. Then solved from the Boltzmann equation to the first order approximation, the conductivity σ can be found to be

$$\sigma = \frac{ne^2\tau}{m} \tag{2.1}$$

For a sample with sparse and random distributed impurities, the mean free time of elastic scattering is

$$\tau = 2\pi n_{imp} \int_0^{\pi} (1 - \cos\theta) S_{imp}(\theta) \sin\theta d\theta \tag{2.2}$$

where θ is the difference in angle between the trajectories before and after collision. n_{imp} is the the density of impurities and S_{imp} is the sample cross section perpendicular to the current [18]. The conductance can be extracted from the Boltzmann equation as

$$G = \frac{s}{L}\sigma(\mu, ...) \tag{2.3}$$

where s is the cross-section perpendicular to the current and L is the sample length along the current direction, μ is the chemical potential. Thus, in the classical electron transport model, Ohm's law can fully describes the picture.

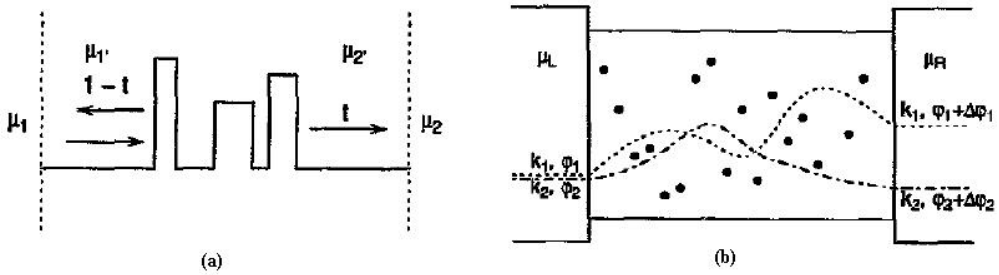

Figure 2.3: (a) The simplest model of a resistor comprises reservoirs, which source and sink current as well as mark the voltage drop across the sample connected by non-scattering leads to a sample which is characterized by a disordered lattice potential. (b) The more general model of a resistor allows the carriers to take more than one path or channel through the disordered potential (represented by the random array of dots). carriers emitted at energy $e\mu_L$ are transmitted through to μ_R at the same energy but (possibly) into a different channel.[6]

In the simplest model of conductor, the sample is modeled as a strictly one-dimensional wire (shown in figure 2.3(a)) connecting two perfect leads serving as reservoirs that emit particles at energies of chemical potential $\mu \pm k_B T$. Related to the transmission coefficients, the conductance can be inferred as [19]

$$G = I_{1\to 2}/(\mu_1 - \mu_2) \tag{2.4}$$

and in convenient natural units,

$$g \equiv \frac{G}{e^2/h} = \Im \tag{2.5}$$

where $\Im$ means the probability for an electron from the left reservoir to the right one and the unit $1/\Omega$ has been dropped. A more general model is shown in figure 2.3(b), where there are multi-channels for carriers. Then g can be reformulated in terms of transmission matrix [20]

$$g = Tr(tt^{+}) \tag{2.6}$$

where the matrix element t_{ij} is the amplitude to depart μ_L in channel i and reach μ_R in channel j.

2.1.2.2 Simplified Ferromagnetic Band Structure: sd Model

The electronic band structure of ferromagnetic transition metals is more complicated than normal metals. It's typically a spin dependent band structure involving electrons from s, p and d bands. There exist approaches for calculating band structure which can be extended to theories of transport. However, to understand basic physical mechanisms it is usually desirable to work with the simplest possible model which contains the necessary ingredients. For the problem of transport in ferromagnetic systems, the sd model is the most commonly used theory of this kind. Originally introduced by Mott [21], the *sd* model is now widely used in ferromagnetic transport models.

Most ferromagnetic metals have s and d bands. The d bands are usually regarded as localized. This is because the d bands are relatively flat, then its effective mass tensor

$$m_{ij}^{*} = \hbar^2 \left[\frac{\partial^2 \varepsilon(k)}{\partial k_i \partial k_j} \right]^{-1} \tag{2.7}$$

has large elements, which means the mobility of d bands is low. The s bands with the normal parabolic structure have a smaller effective mass due to its higher curvature. Thus, s electrons take most part of the current. The special feature of ferromagnets is that the exchange coupling between electrons induces a splitting effect in their band structure. While s electrons are responsible for conduction, d electrons are responsible for magnetization. Thus, the magnetization is proportional to the difference between spin-up and spin-down d electrons.

$$M \propto N_{\uparrow} - N_{\downarrow} \tag{2.8}$$

The proportionality constant is the Bohr Magneton μ_B. Note that an external field can either enhance or weaken the band splitting effect, thus changes the magnetization M.

A diagram of ferromagnetic metal band structure is shown in figure 2.4. From this diagram, we can see that the spin-up electrons are the majority spin and the spin-down electrons are the minority spin. But it is not necessarily the majority carrier is the majority spin. Since the spin-up (majority) d subband lies almost below the Fermi energy, there are few available states at Fermi level. On the contrary, the spin-down (minority) d subband has a large density of states at Fermi level. Since most scattering processes are spin-conserved, then spin-down s electrons can scatter into not only available spin-down s subbband states, but also available spin-down d subband states. On the other side, spin-up s electrons basically have only one choice, scattering into other available spin-up s states. Consequently, the dominant contribution to resistivity is made by the sd scattering.

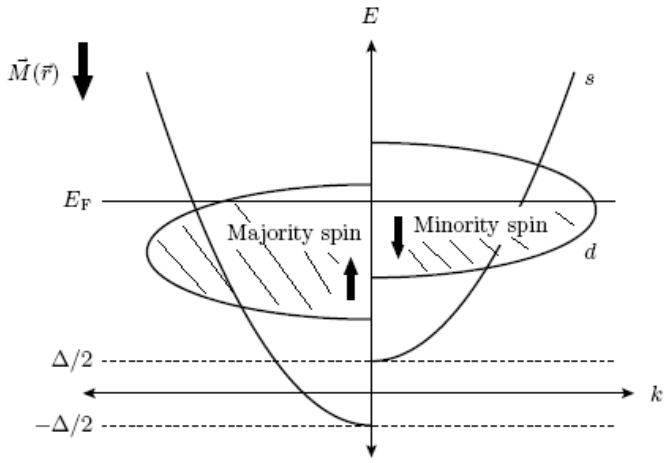

Figure 2.4: Diagram showing the spin-dependent band structure for ferromagnetic materials. The s band has a parabolic dispersion relation, with a spin-split potential energy Δ resulting from the sd exchange interaction. The d band has a narrow form, with a significant difference in the number of up and down states at the Fermi energy. The arrows denote the electron spin direction in each sub-band with respect to the magnetization direction.

2.2 Magnetoresistance Effects in Ferromagnets

The magnetoresistance(MR) is an essential effect exhibited in both normal metals and ferromagnetic materials. It describes the dependence of the resistance with external magnetic field. This effect was first found in bulk ferromagnetic metals.

2.2.1 Magnetoresistance

2.2.1.1 Magnetoresistance in Normal Metal

The first discovery of MR was by Lord Kelvin in 1856. He found a 0.2% increase in resistance R of iron when he applied a magnetic field parallel to the direction of the current and a 0.4% decrease when he applied the field perpendicular to the current. He defined the change in resistance with the external magnetic field H as:

$$\frac{\Delta\rho}{\rho} = \frac{\mathrm{R(H)} - \mathrm{R(0)}}{\mathrm{R(0)}} \tag{2.9}$$

The force F on a particle of charge q moving at velocity v in an electric field E and magnetic induction B can be calculated by the Lorentz force law, as shown in equation 2.10:

$$F = q(E + v \times B) \tag{2.10}$$

Some interesting motions will occur due to the Lorentz force. One of them is show in figure 2.5. It seems this effect must have some special effects on the electron transport, but actually, this effect is not so strong as people have expected. The Lorentz force induced magnetoresistance is referred to as ordinary magnetoresistance (OMR).

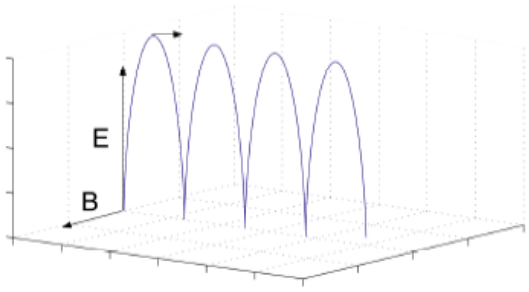

Figure 2.5: A particle initially at rest exhibits cycloid motion when an electric field E and magnetic induction B are applied[24]

The Hall effect is a direct consequence of the Lorentz force on moving charge carriers[22]. It was accidentally discovered in 1879 in Hall's experiment, where he meant to look for a totally different effect. The layout of Hall's experiment is shown in figure 2.6(a). A current density j_x is flowing through a long, thin sample, while a magnetic induction B_z is present. According to the Lorentz force law, the charge carriers experience a force in $\hat{y}$,

$$F_y = qv_x \times B_z = qvB \tag{2.11}$$

which induces a deflection of the carriers' motion (see figure 2.6(b)). Then an electric field E_y in $-\hat{y}$ is built up. Since the effect of E_y on the charge carriers is opposite to F_y, a steady state will be reached (see figure 2.6(c)) when

$$qE_y = F_y \tag{2.12}$$

Then E_y can be calculated from 2.11 and 2.12 to be

$$E_y = vB \tag{2.13}$$

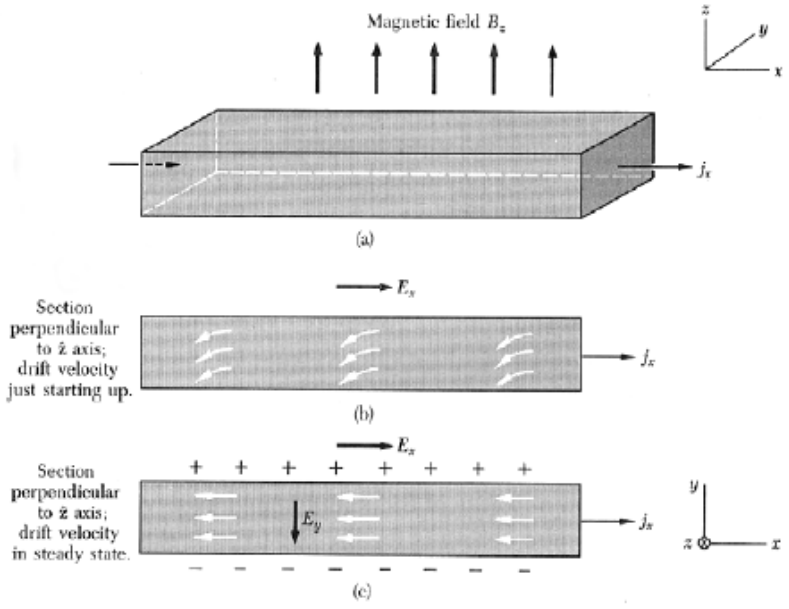

Figure 2.6: Diagram of Hall Effect[22]

A quantitative measure of the deflection of the charge carrier is the Hall angle θ_H, which physically represents the angle between the applied electric field and the Lorentz-deflected current, i.e.

$$\tan\theta = \frac{E_y}{E_x} \tag{2.14}$$

where E_x is the electric field generating j_x. Then

$$E_x = j_x/\sigma = nvq/\sigma \tag{2.15}$$

where n is the number density of carriers. Then based on equation 2.13, 2.14 and 2.15,

$$\tan\theta_H = \frac{\sigma B}{nq} \tag{2.16}$$

Practically, the Hall coefficient R_H is defined as

$$R_H \equiv \frac{1}{nq} = \frac{E_y}{j_x B_z} \tag{2.17}$$

It is a more useful parameter for measurement to get the density of the charge carriers and find out the carrier type according to its sign. It will be seen in a following section about the domain wall resistance, that Hall effect can induce some extra resistivity of samples with strip domains.

For normal metals, the magnetoresistance is experimentally found to be proportional to B^2 in small fields and proportional to B in large fields. The Two-Band model [23] is the simplest one to explain these experimental results. In this model, the current density j is split into two separate current densities: one for the electrons j_e and the other one for the holes j_h. It's called "Two-Band" because in most transition metals there are electrons carrying current from the s band and holes carrying current in the d band [23]. j_e and j_h are deflected away from E with Hall angles θ_e and θ_h respectively, while the total current density j is deflected by Hall angle θ. The electric field for each current density is the projection of E onto each current direction $E\cos\theta_e$ and $E\cos\theta_h$. The by Ohm's law, the conductivities of the total current and each band are

$$\sigma = \frac{j}{E\cos\theta}, \sigma_e = \frac{j_e}{E\cos\theta_e}, \sigma_h = \frac{j_h}{E\cos\theta_h} \tag{2.18}$$

Then $\sigma_0 = \sigma_e + \sigma_h$ is the original conductivity.

Using the lowest order approximations that $\sigma_e = \sigma_h = \frac{1}{2}\sigma_0$ and $n_e = n_h = n$, it can be obtained that [24]

$$\frac{\Delta\rho}{\rho_0} = \left(\frac{\sigma_0}{2ne}\right)^2 B^2 \tag{2.19}$$

Clearly, equation 2.19 predicts the proportionality $R \propto B^2$ of normal metal magnetoresistance at small fields observed experimentally. Without $n_e = n_h = n$, the model also roughly predicts linear scaling at high fields. The bottom line is this result does provide some insight for the effects of the Lorentz force on the dynamics of the charged carriers in non-magnetic metals.

Magnetoresistance is not a phenomenon that can be observed in every normal metal at all conditions. From materials point of view, normal metals should be very clean in order

to see magnetoresistance. Practically, the following conditions must be satisfied to make magnetoresistance observable:

$$\omega_c > f_e \tag{2.20}$$

where,

$$\omega_c = \frac{eB}{m} \tag{2.21}$$

$$f_e = \frac{v_F}{l} \tag{2.22}$$

is the electron scattering rate. Even in a strong field of 10 T, the electron mean free path need to be as long as 1 μm, which is possible only in very clean samples.

2.2.1.2 Magnetoresistance of Ferromagnets

In ferromagnetic materials, there are generally three types of magnetoresistance effects: (1) the electrical resistance changes related to changes in magnetization at a fixed temperature; (2) the electrical resistance changes related to changes in magnetization due to temperature changes; (3) the electrical resistance changes related to changes of the angle between electrical current and magnetization. The third one is the so call anisotropic magnetoresistance (AMR), which will be discussed in more detail in a following section.

Perrier proposed in 1927 that the temperature dependence of resistance for ferromagnets was due to thermal effects on magnetization [25]. Besides, there are still many other competing theories for the wide variety of temperature dependence observed. The other two types of magnetoresistance were first approached by Smit in 1951 [15]. These effects are indicated in figure 2.7.

The Magnetoresistance effect is of great interest for researchers in both applied and fundamental science. On the application side, the magnetic recording industry rely heavily on this effect. Fundamentally, probing the reasons for the anisotropy of the magnetoresistance becomes a problem rich in quantum mechanics and solid state physics.

In ferromagnets, the magnetoresistance can be observed more easily. Most importantly, ferromagnetic materials can exhibit magnetoresistance even in a dirty ferromagnet, where $\omega_c << f_e$.

2.2.2 Anisotropic Magnetoresistance

Since more than a century ago a number of studies have been carried out on the electric transport properties in ferromagnetic metals. People have revealed many remarkable features which are not present in normal metals. One of the most notable would be the hysteretic and anisotropic behavior of the resistance in the magnetic field (magnetoresistance) observed at small magnetic field. The hysteretic behavior of the magnetoresistance indicates that the resistivity depends on the magnetization M. The electrical resistivity ρ, as a function of the field H, has also been observed to be dependent on the angle between the direction of electrical current and orientation of magnetization. The resistivity difference between $\rho_{//}$ and $\rho_{\perp}$ is the anisotropic magnetoresistance (AMR), where // and $\perp$ represent the relative direction between the electrical current and magnetization.

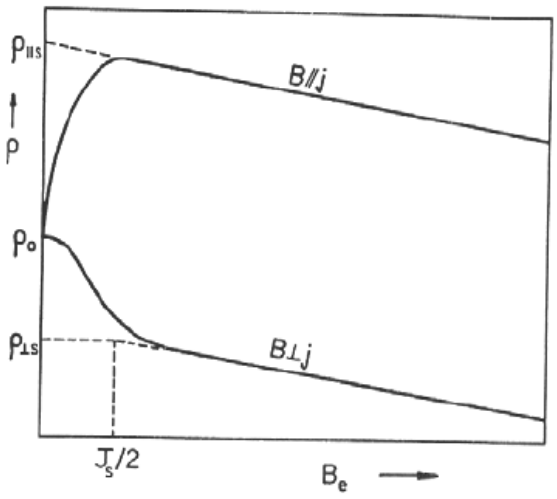

Figure 2.7: Characteristic dependence of resistance R on magnetic induction Be. Note in particular the difference in resistance observed for the two different orientations of in plane magnetic induction B relative to current density j[15]

AMR is an essential effect of ferromagnetic materials. It has been successfully used in industry for magnetic field detectors. The AMR ratio can be greater than 5% for Ni-Fe and Ni-Co at room temperature, and this ratio can be affected by many factors, such as sample thickness, grain size, etc. William Thomson [26] fist discovered AMR in ferromagnetic metals in 1857.

One of the experimental results on AMR is shown in figure 2.7, which exhibits a clear

difference between $\rho_{//}$ and $\rho_{\perp}$. Besides, as the external magnetic field increases, both $\rho_{//}$ and $\rho_{\perp}$ decrease uniformly. The AMR ratio is defined as

$$\frac{\Delta\rho}{\rho_{av}} = \frac{\rho_{//} - \rho_{\perp}}{\frac{1}{3}\rho_{//} + \frac{2}{3}\rho_{\perp}} \tag{2.23}$$

In real experiments, the resistivity measured at zero field ρ_0 is not ρ_{av}, but since the difference between them is negligible, we can use either one of them. In a single domain film sample, the resistivity is found to be [4]

$$\rho(\theta) = \rho_{\perp} + \Delta\rho\cos^2\theta \tag{2.24}$$

where θ is the angle between electrical current I and magnetization M.

The formation of AMR effect can be started from Mott's [21] model based on *sd* band scattering which we already mentioned in *section*2.1.2.2. The essential assumptions in his model are: first, the *s* electron carries most of the current since its effective mass m_s^* is approximately equal to the free electron mass m_e, while the effective mass of the *d* electron m_d^* is much greater than m_e; second, *sd* scattering is dominant due to the much larger density of states of *d* electrons than *s* electrons at Fermi level, thus *sd* scattering contributes to the resistivity much greater than *ss* scattering. Based on these assumptions, Mott managed to solve the coupled Boltzmann equation and obtained two relaxation times τ_s and τ_d, which are constant and isotropic. Approximately,

$$\frac{1}{\tau_s} = \int P_{k,k'}^{sd} ds' = \frac{\pi}{\hbar} N_d(\varepsilon_F) \int \left| V_{k,k'}^{sd} \right|^2 \sin\theta' d\theta' \tag{2.25}$$

where θ is the angle between k and k'. The conductivity is

$$\sigma = \frac{n_s e \tau_s}{m_s^*}. \tag{2.26}$$

where τ_s is inversely proportional to $N_d(\varepsilon_F)$, and m_s^* is approximately the free electron mass.

At temperatures well below Curie temperature, assuming the majority and minority spin *s* electrons contribute to the conductivity independently would be a reasonable approximation. Then the total conductivity can be simplified and written as

$$\sigma = \sigma_{s+} + \sigma_{s-} \tag{2.27}$$

This is referred to as the "two-current" model [4]. Where "+" represents minority spin electrons and "-" represents majority spins. Additionally, assuming the additivity of the probabilities of *sd* scattering and *ss* scattering is equivalent to solving the limiting cases of the coupled equations. Then the intermediate case can be written as

$$\frac{1}{\tau} = \frac{1}{\tau_{ss}} + \frac{1}{\tau_{sd}} \tag{2.28}$$

Combine it with the "two-current" model, one can get [4]

$$\sigma = \frac{ne^2}{m_s}\left[\frac{1}{\frac{1}{\tau_{ss}} + \frac{1}{\tau_{s+,d+}}} + \frac{1}{\frac{1}{\tau_{ss}} + \frac{1}{\tau_{s-,d-}}}\right] \tag{2.29}$$

where $n \equiv n_{s+} = n_{s-}$, and $\tau_{ss} \equiv \tau_{s+,s+} = \tau_{s-,s-}$. Since d bands are exchange split, $\tau_{s+,d+}$ and $\tau_{s-,d-}$ are expected to be different.

Based on Mott's model, AMR must be a consequence of anisotropic scattering if *sd* scattering is dominant in the transition-metal conductivity. Generally, an isotropic scattering potential with lower-than-cubic-symmetry wavefunctions is considered a likely mechanism of anisotropic scattering. Smit [15] proposed that the spin-orbit interaction lowers the symmetry of wavefunctions. In a radial electrostatic potential, the spin-orbit interaction can be represented as

$$H_{S.O.} = KL \bullet S \tag{2.30}$$

where K is a constant related to nuclear parameters, L is the orbital angular momentum of the electron, and S is the spin magnetic moment of the electron. Equation 2.30 makes an energy contribution to d band electrons, while its magnetization is in favor of certain crystallographic directions, leading to the coupling between d electron spin and its orbital motion. The the new wavefunctions ψ_d^1 can be calculated in terms of ψ_d^0, the wavefunctions without taking account of spin-orbit interaction. Since the spin-orbit interaction mixes both spin-up and spin-down states, ψ_d^1 have lower-than-cubic symmetry. The relaxation times are represented as

$$\frac{1}{\tau_{s\pm,d}} \approx \frac{2\pi}{\hbar} N_d(\varepsilon_F) \left| \int \psi_{s\pm}^* V_{scatt} \psi_d^1 d\tau \right|^2 \tag{2.31}$$

where $d\tau$ denotes both spatial and spin coordinates. Choosing ψ_d^0 as $xyf(r)$ and discarding the $L_Z S_Z$ term in $L \bullet S$, Smit [15] found $\rho_{//} > \rho_\perp$ consistent with experimental observations.

In potter's calculation [27], he chose Ψ_d^0 obtained by tight-binding method, assumed d band to be nearly full and $V_s catt \propto \frac{e^2}{r} e^{-qr}$ and found that

$$\frac{1}{\tau_{s+,d}} \propto \cos^2(\theta) - \cos^4(\theta) \tag{2.32}$$

and

$$\frac{1}{\tau_{s-,d}} \propto 1 - 2\cos^2(\theta) + \cos^4(\theta) \tag{2.33}$$

where θ is the angle between current and magnetization. In a polycrystalline sample, higher order dependence averages to zero, then only $\cos^2(\theta)$ dependence left. This is consistent with equation 2.24. These results indicate

$$\frac{1}{\tau_{s-,d}(\theta = 0)} < \frac{1}{\tau_{s+,d}(\theta = \pi/2)} \tag{2.34}$$

and

$$\frac{1}{\tau_{s+,d}(\theta = 0)} > \frac{1}{\tau_{s+,d}(\theta = \pi/2)} \tag{2.35}$$

which imply that if the anisotropy is due to majority spin electrons, then $\rho_{//} < \rho_{\perp}$, otherwise $\rho_{//} > \rho_{\perp}$ if the anisotropy is due to minority spins. The AMR ratio was found to be a function of four parameters, i.e.

$$\frac{\Delta\rho}{\rho_{av}} = f\left(\beta\frac{N_s(\varepsilon_F)}{N_d(\varepsilon_F)}, \frac{K}{\varepsilon}, \frac{K}{2\gamma}, \frac{K}{2\gamma + e}\right) \tag{2.36}$$

where ε is the splitting between the uppermost two d bands of like spin, 2γ is the exchange splitting, assumed to be uniform. N_s/N_d provides the relative importance of ssscattering and sd scattering. $\Delta\rho/\rho_{av}$ can be either positive or negative according to 2.34 and 2.35, its sign will depend on the values of these four parameters.

2.2.3 Domain Wall Resistance

Domain wall is the transition region between domains with different magnetization directions. Its scale depends on the sample shape, the exchange energy and magnetic anisotropy energy of the material. Domain wall widths are between 1 nm to 200 nm in most cases[5]. Inside a domain wall, magnetization electron spins rotate spatially within the finite domain wall width. Fig 2.8 shows a diagram of domain wall.

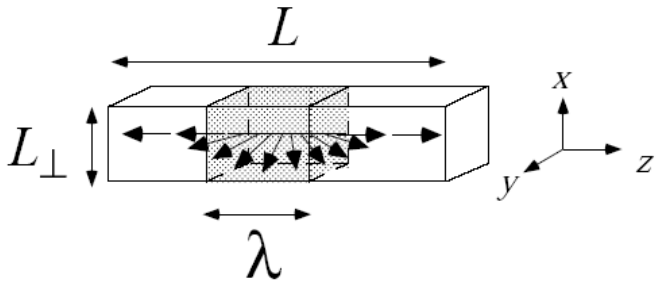

Figure 2.8: A configuration of a domain wall in a mesoscopic wire[36]

Domain wall resistance (DWR) was found in early magnetotransport experiments on single crystal Fe whiskers [28]. At low temperatures, the resistivity of Fe whisker drops significantly while a saturating magnetic field is applied. The applied magnetic field removes domain walls, and consequently changes the multidomain Fe into a singledomain state. Cabrera and Falicov proposed the first model of domain wall scattering [29]. Considering the reflection of conduction electrons by the effective potential within the domain wall, they found the reflection probability to be proportional to $e^{-\delta/\lambda}$, where δ is the domain wall width and λ is the Fermi wavelength. For a sample with domain wall width of 10 nm and Fermi wavelength of 0.1 nm, the reflection rate is so small that the resistance due to domain walls is considered to be negligible.

As the technique to fabricate thin film sample advances, more precise experimental measurements of DWR have emerged. Both positive and negative DWR have been observed experimentally [30, 31, 32, 33, 34]. Meanwhile, different models [35, 2, 36] proposed by theorists also give support to either positive or negative contributions by DWR to sample resistance.

In 1996, Gregg *et al.* [30] found DWR effects analogous to giant magnetoresistive effects(GMR) in their chemically homogeneous magnetic thin films, where a 180° domain wall resembles the non-magnetic layer in a traditional GMR system. In ferromagnets, spin-dependent potentials and spin relaxation times are different for spin-up and spin-down electrons. This is critical to understand not only the GMR effects, but also the domain wall effects on resistivity. The resistivity of one spin channel is usually lower than the other in a

ferromagnetic metal, so there exists a short circuit in a uniformly magnetized sample. When domain walls are present, mixing of the spin channels is caused by scattering within the wall, which removes the "short circuit" effect partially and increases the resistivity inside the domain wall region [35]. Using the same Hamiltonian [35] used in understanding GMR to treat the resistivity due to domain walls, Levy and Zhang [35] found their results to be consistent to Gregg's experimental findings. When current is parallel to the domain walls (CIW), magnetoresistance ratio R is found to be:

$$R_{CIW} \equiv \frac{\rho_{CIW} - \rho_0}{\rho_0} = \frac{\xi^2}{5} \frac{(\rho_0^{\uparrow} - \rho_0^{\downarrow})^2}{\rho_0^{\uparrow}\rho_0^{\downarrow}} \tag{2.37}$$

The parameter $\xi = \hbar v_F/(J\delta)$, where δ is the domain wall width, J is the internal exchange energy. v_F is the Fermi velocity. $\rho_0^{\uparrow}$ and $\rho_0^{\downarrow}$ are the resistivity of spin-up and spin-down channels respectively. Clearly, if $\rho_0^{\uparrow} = \rho_0^{\downarrow}$, $R_{CIW} = 0$, i.e. domain walls do not contribute additional resistance. When current is perpendicular to the domain walls (CPW), the resistivity ρ_{CPW} is found to be:

$$\rho_{CPW} = \rho_0[1 + \frac{\xi^2}{5} \frac{(\rho_0^{\uparrow} - \rho_0^{\downarrow})^2}{\rho_0^{\uparrow}\rho_0^{\downarrow}} (3 + \frac{10\sqrt{\rho_0^{\uparrow}\rho_0^{\downarrow}}}{\rho_0^{\uparrow} + \rho_0^{\downarrow}})][35] \tag{2.38}$$

Taking typical Co. parameters, $k_F = 1 \overset{o}{A}^{-1}$, $J = 0.5$ eV and $\rho_0^{\uparrow}\big/\rho_0^{\downarrow}$ in the range of 5-20, they found the CPW magnetoresistance is between 2% and 11% [35]. This is consistent with the Gregg's experimental finding of 5% [30].

On the contrary , Tatara and Fukuyama found the effect of domain wall is to reduce resistivity from their calculation based on the linear response theory [2]. At low temperatures, domain wall scattering is the major source for decoherence, which suppresses weak localization and consequently reduces sample resistance. In their model, Tatara and Fukuyama have calculated both classical and quantum contributions of domain walls on resistivity. In a disordered case, the ratio of the domain wall contribution to the full resistivity is obtained to be:

$$\frac{\Delta\rho_{\mathrm{w}}}{\rho} = \frac{1}{\left[1 - (\sqrt{3}\pi/(k_F L_{\perp})^2)(1/\sqrt{\kappa_{\varphi}})^2)\right]} \left[\frac{3}{2}\frac{n_w}{k_F^2\lambda} - \frac{\sqrt{3}\pi}{(k_F L_{\perp})^2}\left(\frac{1}{\sqrt{\kappa_{\varphi}}} - \frac{1}{\sqrt{\kappa_{\varphi} + \kappa_w}}\right)\right] [36] \tag{2.39}$$

The second term in the square bracket is the quantum contribution, which reduces the resistivity.

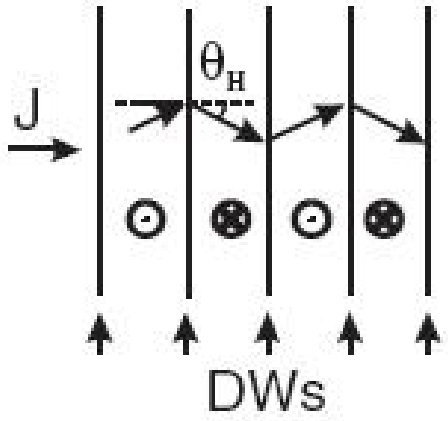

Figure 2.9: A macroscopic Hall effect mechanism (view in the z=0 plane)[5]

The domain wall resistance can be disguised by some extrinsic magnetoresistance, such as ferromagnetic resistivity anisotropy, diamagnetic effect and a Hall effect mechanism, which are related to the domain configurations [5]. Berger [37] showed a mechanism based on Hall effect can give a higher resistivity for a multidomain sample than a saturated sample. In the CPW geometry, the Hall effect leads to a current deflection near the domain walls in strip domain material, provided the sample width is larger than the domain subdivisions. This deflection makes the current zig-zag the sample (see figure 2.9), since the Hall angle changes sign in alternating domains [37]. It has been found by Berger [37] that this zig-zaging current leads to a resistivity gain of order $(\rho_{xy}/\rho_{xx})^2$, which is the Hall angle squared. In other words[37],

$$\delta\rho = \rho_s \left|\beta\right|^2 \sin^2\theta \tag{2.40}$$

where ρ_s is the resistivity in a saturated sample where the domain wall is absent, β is the tangent of Hall angle, and θ is the angle between the electric current and the domain wall plane. Then in a CIW geometry, where the current is parallel to the wall plane, i.e., $\theta = 0$, there is no resistance gain due to this effect.

2.3 Quantum Corrections in Mesoscopic Electron Transport

As the ability to fabricate small samples and to conduct electric transport experiments at very low temperatures advances, many innovative phenomena have been observed experimentally, such as conductance fluctuations, weak localization effect, and so on. While the classical mechanics fails to provide compatible explanations, people are forced to employ a wave mechanics to describe those new transport problems. Surprisingly, quantum mechanics starts to play its role in mesoscopic scale, which is far above the atomic scale. Practically, the macroscopic approach, such as ensemble averaging, breaks down as long as the sample-to-sample differences only due to microscopic difference (e.g. the impurity locations) become measurable [6]. In this regime, the electron should be regarded as a wave having an amplitude and a phase instead of a particle.

Mesoscopic effects can be observed in weakly disordered samples at low temperatures. A phase coherence length (L_φ) much longer than the mean free path (l) can be achieved at very low temperatures. The reason is that elastic collisions do not destroy phase coherence and density of phonons and other thermal excitations (inelastic collisions) are very small at low temperatures[6]. Besides, the defects in the the conductor lattice tend to localize the electron wave to prevent its transport. Only when the sample size L is much less than the localization length L_C, the sample conductance can be appreciable[38]. This is the so-called weakly localized regime. In this regime, quantum interference is one of the most important mechanisms lying under many interesting phenomena.

2.3.1 Aharonov-Bohm Effect

In classical mechanics, when a charged particle is passing through an electrical field free area with magnetic field $B = 0$, its motion will remain unchanged. In 1959 , Aharonov and Bohm's experiments showed something distinct [39]. In the experiment, a beam of coherent electrons passes over a infinitely long solenoid. The flux inside the solenoid is Φ while a current flowing through the solenoid. The electron beam splits into two beams across the solenoid and and recombines back to one beam showing a clear phase shift in the

interference pattern. The experiment diagram is shown in figure 2.10. This is the famous Aharonov-Bohm (AB) effect.

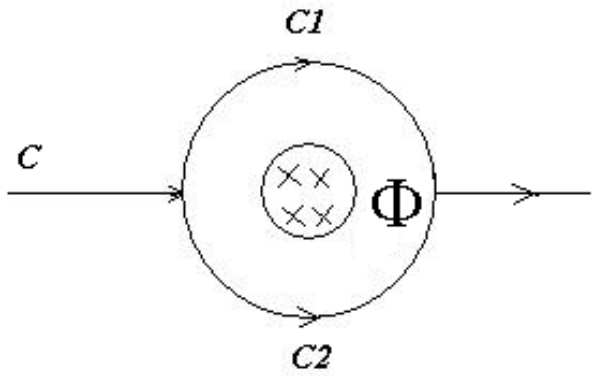

Figure 2.10: Diagram of the Aharonov and Bohm experiment. A beam of phase coherent electrons C splits into beams C_1 and C_2, which enclose the magnetic flux Φ generated by a infinitely long solenoid.

AB effect is a quantum effect. Electrons should be treated as waves instead of particles as in the classical mechanics. The phase change of a electron beam after undergoing a path where the electromagnetic potential is zero is calculated as:

$$\varphi = \int_c \vec{k} \cdot d\vec{r} = \int_c \frac{m\vec{v}}{\hbar} \cdot d\vec{r}, \tag{2.41}$$

where

$$\vec{p} = m\vec{v} = \hbar\vec{k}$$

is the momentum of electrons. When there is a current flow through the solenoid, although the magnetic field B outside the solenoid is zero, the electromagnetic potential $\vec{A}$ is not zero. The momentum need to be replaced by the canonical momentum, which is:

$$\vec{P} = \vec{p} + q\vec{A} = m\vec{v} - e\vec{A} \tag{2.42}$$

Then the two split electron beams along path C_1 and C_2 have the additional phase difference:

$$\begin{aligned} &\varphi_1 - \varphi_2 = \textstyle\int_{C_1} \frac{(m\vec{v}-e\vec{A})}{\hbar} \cdot d\vec{r} - \int_{C_2} \frac{(m\vec{v}-e\vec{A})}{\hbar} \cdot d\vec{r} \\ &= \tfrac{e}{\hbar}[\textstyle\int_{C_2} \vec{A} \cdot d\vec{r} - \int_{C_1} \vec{A} \cdot d\vec{r}] = \tfrac{e}{\hbar} \oint_C \vec{A} \cdot d\vec{l} \end{aligned} \tag{2.43}$$

and

$$\oint_C \vec{A} \cdot d\vec{l} = \int_S (\vec{\nabla} \times \vec{A}) \cdot d\vec{S} = \int_S \vec{B} \cdot d\vec{S} = \Phi \tag{2.44}$$

So the phase shift is equal to the flux enclosed by the two paths, i.e. the line integral of the electromagnetic potential $\vec{A}$ along the closed loop. Since the magnetic field B are both zero outside the solenoid before and after the current is flowing, it is the electromagnetic potential $\vec{A}$ that induces the phase shift. Thus, the electromagnetic potential $\vec{A}$, which cannot be measured directly as the electrical potential, is found to be directly related to the quantum behaviors of electrons.

2.3.2 Weak Localization Effect

Weak localization(WL) is a widely studied effect. It occurs in disordered samples at very low temperatures, where the number of thermal excitations (such as phonons) is very small. Since elastic collisions don't destroy phase coherence, the coherence length L_φ becomes longer due to the decreasing probability of inelastic collisions as the temperature decreases. If the coherence length is much longer than the electron's mean free path length, i.e. $L_\varphi >> l$, let's consider a pair of trajectories, which are clockwise and counterclockwise around the same loop 2.11. Since the lengths of the loop in both directions are the same, the electron wavefunctions will interfere constructively at the origin, provided L_φ is long enough to retain phase coherence along the loop. This process is called coherent back scattering and a standing wave is set up around the loop. Since standing waves don't carry current, less current goes away from the origin, thus conductance is suppressed by the quantum interference. This is the so called 'weak localization' effect [6]. As temperature decreases, L_φ increases so that larger loops contribute to the quantum interference and sample resistance increases. The pair of time-reversed trajectories are sometimes called 'cooperons' since they are analogous to the Cooper pairs of electrons in superconductors.

For $\omega << 1/\tau$ (small frequencies), with the quantum interference correction, the change in Drude conductivity σ_0 is calculated [40] to be:

$$\Delta\sigma \equiv \sigma - \sigma_0 \propto -\int \frac{d^d q}{\tau D q^2 + \tau/\tau_\varphi - i\omega\tau} \tag{2.45}$$

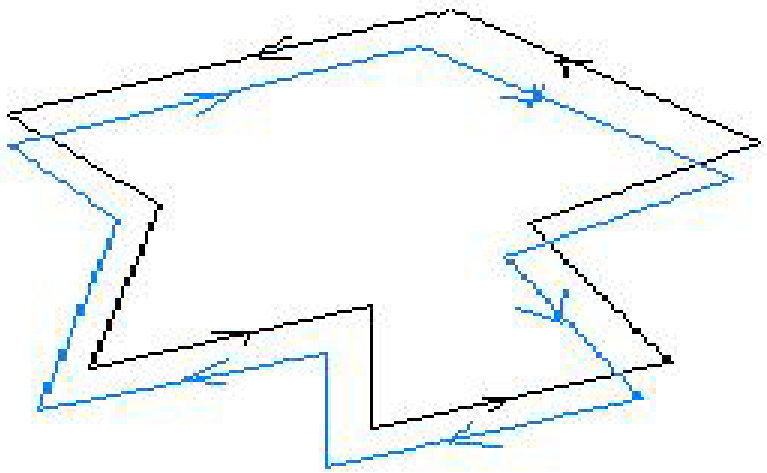

Figure 2.11: Diagram of weak localization. A pair of clockwise and counterclockwise trajectories are shown in blue and black respectively.

where $q = k_1 + k_2$ is the sum of initial and final momenta, d is the spatial dimensionality, τ_φ is the mean time between collisions destroying the electron phase, and ω is the frequency of the measurement. Sizes of the loops contributing to the corrections are limited by the phase coherence range of the sample. As the effective dimensions of the sample decreases, one or more of the integrations over dq is cut off by the sample dimension instead of L_φ. Thus weak localization effect is stronger in lower dimensions.

Weak localization effect can be destroyed by applying an external magnetic field, because the standing waves depend on the time-reversal symmetry between the pair of trajectories. The phase of one trajectory is advanced while the other one is retarded by a magnetic flux threaded through the back-scattering loop due to AB effect. A magnetic flux $\Phi = \vec{B} \bullet \vec{S} \approx h/2e$ passing through the loop can dephase the pair substantially. For a single loop, its resistance can be measured to be oscillating with period $h/2e$ [41]. In a thin film metal sample, since all back-scattering loops of sizes up to L_φ^2 contribute to the WL and different loops enclose different amounts of flux, the total WL signal is gradually reduced to zero by a magnetic field $B = h/2eL_\varphi^2$ [6].

2.3.3 Conductance Fluctuations

At low temperatures, conductance of mesoscopic samples will exhibit noise-like but reproducible fluctuations as a function of magnetic field or chemical potential. The phenomena have been observed in a variety of mesoscopic devices (see figure 2.12). This kind of fluctuations is sample-specific, so the sample behavior can no longer be characterized by the ensemble average. It is the quantum interference that plays the critical role in this regime. The conduction electron cannot be treated as a billiard ball any more, but rather as a wave with an amplitude and a phase. It has been found experimentally and theoretically that the magnitude of the fluctuation is of the order of the conductance quantum, if $L < L_\varphi$.

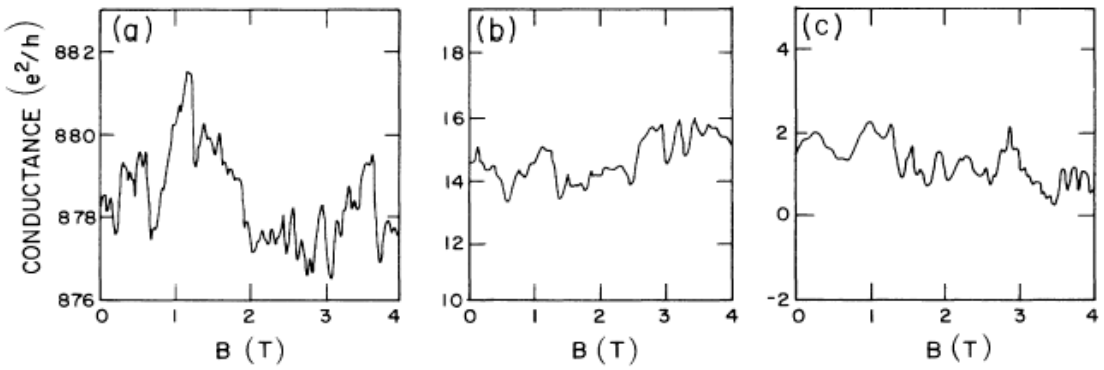

Figure 2.12: Comparison of aperiodic magnetoconductance fluctuations in three different systems (a) 0.8-μm-diam gold ring, (b) Quasi-1D silicon MOSFET, (c) Numerical calculation for an Anderson model . conductance is measured in units of e^2/h, magnetic field in $Tesla$. Note that fluctuations are of the same order although the background conductances are of 3 order difference[49].

The conductance fluctuations were firstly observed by Umbach *et al.* [42] in their experiments on the magnetoresistance of a small gold ring below 1 K. They also found that this kind of conductance fluctuations were enhanced at lower temperatures in their following experiments [43]. Based on numerical simulation of diffusive transport in disordered samples, Stone [44] provided a theoretical explanation to this phenomena. Additionally, the *rms* value of the conductance fluctuations to be e^2/h was predicted by Al'tshuler [45] based on transport theory. The mechanism underlying this effect is the quantum interference. In mesoscopic regime, the wave properties of electrons produce constructive or destructive interference between electron waves.

In Landauer's approach [46], the electron transport is regarded as an electron wavefunction scattered by the disorder in the lattice. And the electron transport is modeled using the superposition of all scattered waves. In a phase coherent sample, the electron wavefunction will keep its phase memory along its path through the sample, so the whole conductor can be regarded as a single scatter with the parameter of transmission coefficient T which represents the average probability that an electron can go through this conductor. The total conductance for a one dimensional sample based on this model can be written as:

$$G = 2(e^2/h)T \tag{2.46}$$

For a multidimensional sample, the total current is the sum of the currents through individual channels. Based on Fermi-statistics, these channel are equally populated and contribute to the whole conductance equally. Then the total conductance can be written as:

$$G = 2(e^2/h)Tr(tt^+) = 2(e^2\Big/h)\sum T_{ij} \tag{2.47}$$

where Tr represents the trace of the matrix, T_{ij} is the transmission amplitude from incoming channel i to outgoing channel j, the summation spreads over all possible channels.

Clearly, from equation 2.47, the sample conductance is decided by the transmission coefficients T_{ij} for all available channels to carriers. And the summation in 2.47 is strongly influenced by the quantum interference among electron waves going through different channels. The phase-shift depends on the electron energy and the spatial configurations of elastic scatterers in the lattice , thus the conductance fluctuations can rise from a change in either the electron energy or the locations of lattice imperfections [47](see figure 2.13). An applied bias voltage or an external magnetic field can induce a change in the phase-shift of electron wavefunctions. A bias voltage directly changes the chemical potential of the carriers, and therefore the phase-shift. Thouless [48] showed, for one-dimensional wires at zero temperature, the energy levels in the conduction band have a width

$$E_C \approx \hbar/\tau_f \approx \hbar D\Big/L^2 \tag{2.48}$$

where $D = v_F^2\tau/d$ is the diffusion coefficient in d dimensions., L is the size of the wire, τ_f is the time to traverse the wire. Then as the bias voltage is changed by $|E_C/e|$, the

carrier energy is altered by E_C, which is enough to change the interference between each pair of channels and thus change the conductance completely. For an external magnetic field perpendicular to the direction of current, a change of Φ_0/S in the field can produce a distinct interference pattern, where Φ_0 is the flux quantum and S is the transverse area of the sample.

On the other side, two macroscopically identical mesoscopic samples will exhibit different conductance. This is because macroscopic properties, such as conductance, depend on microscopic details. Even the relocation of one single scatterer can potentially induce a large change in conductance. This effect is stronger in 2-D samples than in 3-D samples. Besides, migration of defects can also change the transmission of channels, thus induces the conductance fluctuations with time.

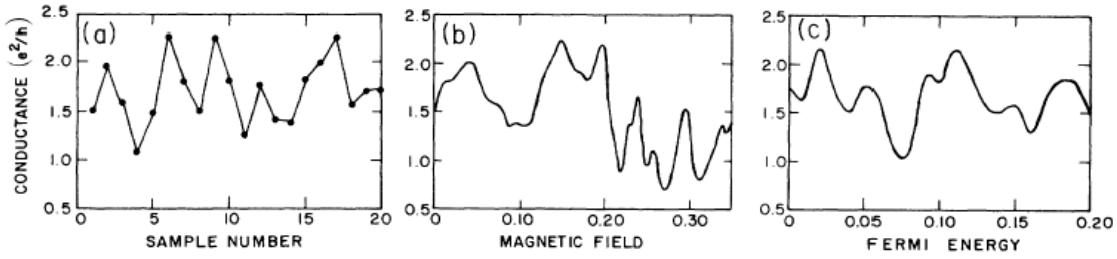

Figure 2.13: Comparison of sample-to-sample fluctuations and fluctuations in $g(B)$ and $g(E)$ in a single sample. (a) g for 20 samples differing only in their impurity configurations. (b) $g(B)$ over a range of about 10 times the field correlation range. (c) $g(E)$ over a range of about 10 times the energy correlation range. The numbers come from the numerical simulation on an Anderson model[49].

To obtain the magnitude of the conductance fluctuations, theorists have employed several sophisticated methods. By means of the Kubo formula, conductance can be calculated in the perturbation theory. The dimensionless conductance g is found to be proportional to L^{d-2}. Lee *et al.*[49] obtained

$$(\Delta g)^2 = g^2 \Big/ L^d \propto L^{d-4} \tag{2.49}$$

As L increases, the fluctuation amplitude vanishes rapidly. This classical estimate treats the transmission channels as independent.

On the contrary, taking account of the correlation functions between conductances,

Maldague [50] found

$$(\Delta g)^2 \propto L^{d-4} \int \frac{d^d q}{q^4} \rightarrow constant \tag{2.50}$$

This does not vanish for any $d < 4$.

In a diffusive sample, the transmissions in individual channels are highly correlated, which is the physical basis for the universal amplitude of fluctuations. For a conductor in this regime, its N transmission channels cannot be treated as statistically independent. Instead, in the overall conductance, it is equivalent to a conductor with N_{eff} independent channels, where N_{eff} is a smaller number than N[51]. The number of effective independent channels N_{eff} was estimated[47]:

$$N_{eff} \approx N\,(l/L)^2 \tag{2.51}$$

where L is the conductor length, and l is the mean free path between collisions. The relation between the average conductance $\langle G \rangle$ and N can be estimated as

$$\langle G \rangle \approx (e^2/h)(l/L)\sqrt{N} \tag{2.52}$$

Then from equation 2.51 and 2.52, it is derived that

$$\langle G \rangle \approx (e^2/h)\sqrt{N_{eff}} \tag{2.53}$$

Consider the conductance of an elementary one-channel conductor. Since the transmission coefficient is between 0 and 1, then

$$\langle g \rangle \approx e^2/h \tag{2.54}$$

and

$$\Delta g_{rms} / \langle g \rangle \approx 1 \tag{2.55}$$

Since N_{eff} channels are independent, we have

$$\Delta G_{rms} / \langle G \rangle \approx (1/\sqrt{N_{eff}}) \Delta g_{rms} / \langle g \rangle \tag{2.56}$$

Substitute equation 2.51 and 2.55 into 2.56, the *rms* value of conductance fluctuation is obtained as:

$$\Delta G_{rms} \approx e^2/h \tag{2.57}$$

,which is a universal constant, independent of conductor geometry and material properties [47]. Now it's clear, for a mesoscopic conductor, that the effective number of channels varies with the transverse area and inversely with the square of the conductor length. This universality can be destroyed by many reasons, such as magnetic effects and spin-orbit interactions.

2.3.4 Electron-electron Interaction Enhancement Effect

Both theoretical and experimental studies on disordered samples at low temperatures have led to quantum corrections to the classical Boltzmann method. As the temperature goes to zero, the quantum corrections become more and more important [52]. Theoretically, weak localization (WL)(discussed in the previous section) and electron-electron interaction (EE) provide explanations to the non-classical behaviors of carriers in electric transport. It is known that, in general, both weak-localization and electron-electron interaction effects could contribute almost equally to the temperature dependent resistivity $\Delta\rho(T)$ of 2-D sheet at low temperatures and in zero magnetic field. But for three-dimensional (3-D) samples (bulk samples), the temperature dependent correction of resistivity in the absence of a magnetic field arises mainly from the electron-electron interaction effects [7, 53]. Thus, it is possible to extract the screening parameter $\vec{F}$ from a high-precision measurements of $\Delta\rho(T)$ in bulk samples [7]. The screening parameter $\vec{F}$ is defined in the EE theory but not understood very well yet. It characterizes the strength of Coulomb interactions between electrons. Because of the enormously complicated interaction effects between electrons, the magnitude of $\vec{F}$ in a real disordered material is extremely difficult to calculate theoretically. In the presence of spin-flip scattering (spin-orbit scattering and spin-spin scattering), the situation becomes even less clear. It has been argued that the contribution from the diffusion channel to electron-electron interaction effects would be suppressed in the presence of strong spin-orbit scattering [54, 55].

Al'tshuler and coworkers [53] have calculated the corrections to low-temperature resistivity and sheet resistances due to electron-electron interaction effects in the weakly disordered

regime and predicted that

$$\frac{\Delta\rho(T)}{\rho_0} = -\frac{0.915e^2}{4\pi\hbar}\left(\frac{4}{3} - \frac{3}{2}\vec{F}^{(3D)}\right)\rho_0\left[\frac{k_BT}{\hbar D}\right]^{1/2} \tag{2.58}$$

where ρ_0 is a reference low-temperature resistivity [taken to be $\rho_0 = \rho(T = 10K)$ in this work], D is the electron diffusion constant, k_B is the Boltzmann constant, and the Coulomb screening parameter is denoted by $\vec{F}^{(3D)}$. They have also predicted that

$$\frac{\Delta G(T)}{G_{00}} = \frac{G(T) - G(T_0)}{G_{00}} = (1 - \vec{F}^{(2D)})\ln(\frac{T}{T_0}) \tag{2.59}$$

in two dimensions, where T_0 is a reference temperature, $G_{00} = \frac{e^2}{2\pi^2}$ is the quantum conductance, and the Coulomb screening parameter is denoted by $\vec{F}^{(2D)}$. These correction terms stem from the diffusion channel involving small momentum and frequency transfers. Physically, there is a suppression of the single-electron density of states at the Fermi level caused by the enhanced electron-electron interactions in the presence of disorder. Such a suppression has been confirmed experimentally by tunneling electronic density of states measurements [56, 57].

According to the theory[53], the electron screening parameter ($\vec{F}^{(3D)}$ or $\vec{F}^{(2D)}$) is a measure of F, which is the dimensionless screened Coulomb potential between electrons averaged over the Fermi surface [53]. Under Thomas-Fermi approximation, $F \to 1$ in the limit of complete screening (or, good metals), while $F \to 0$ in the limit of no screening (or, 'bad' conductors). Al'tshuler *et al.* suggest that poor screening of electrons due to large interaction effects causes a significant rise of low-temperature resistivity (sheet resistance). In general, $\vec{F} \approx F$ in the limit $F \to 1$. If F is not small, in the range $|F| \leq 1$ it can be readily shown that $\vec{F}$ equals F to within $\approx 10\%$ deviation from F . Thus, it should not be critical to distinguish between $\vec{F}$ and F in most experiments. A more detailed explanation of the relation between $\vec{F}$ and F can be found in [7, 53].

CHAPTER III

SAMPLE FABRICATION OF COBALT NANOPARTICLE

Our mesoscopic Co ferromagnetic samples are made by electron beam lithography and high vacuum shadow evaporation techniques. The whole process contains three main steps: (i) Spinning double-layer polymer coating on silicon wafers; (ii) Designing pattern with NPGS software and realizing the pattern on polymer-coated silicon wafer by electron beam lithography; (iii) Depositing metal films in the high vacuum thermal evaporator with shadow evaporation technique.

3.1 Polymer Coating on Silicon Wafers

The first step in our sample fabrication is spin coating. A spinner is the standard equipment to do this job. An excess amount of resist solution is placed at the center of the substrate. Then the substrate is rotated at very high speed provided by the spinner in order to spread the fluid uniformly across the substrate by centrifugal force. The thickness of the coating layer depends on the rotating speed. The higher the speed, the thinner the coating film. The thickness also depends on the concentration of the solution, higher concentration usually leads to thicker film. The coating procedure for one resist layer is generally composed of two steps: the first step is to accelerate the rotating speed of the spinner to a desired speed, the second step is to let the spinner rotate continually at this constant speed for some extra time. The parameters of rotating speed and rotating time can be pre-programmed as recipes and stored in the spinner controller for future usage.

The polymer coating we need for this experiment is a double layer electron beam resist film on a whole piece of silicon wafer. The two kinds of polymer we use are polymethyl methacrylate (PMMA) and copolymer methacrylic acid (MMA). Both are positive electron beam resists having long-chain chemical structures, which means after exposure to the electron beam, the exposed part will dissolve in the developer solution (MIBK:IPA=1:3)

due to the breaking down of their long chains and the unexposed part survive. The reason to have a double layer resist is to make an undercut which is critical to the following shadow evaporation procedure. The top layer is PMMA, the bottom layer is MMA. Since MMA is more sensitive to the electron beam exposure than PMMA, it can be removed by a less dose of electron beam than PMMA. The MMA we use for this experiment is of a higher concentration, thus it can form a thicker layer than those of lower concentration such that the undercut has enough depth. Having the bottom MMA layer, we can make an undercut by choosing appropriate dose to get rid of MMA only and let PMMA stay. The undercut makes shadow evaporation possible. A schematic drawing of the double layer coating and an undercut is shown in figure 3.1.

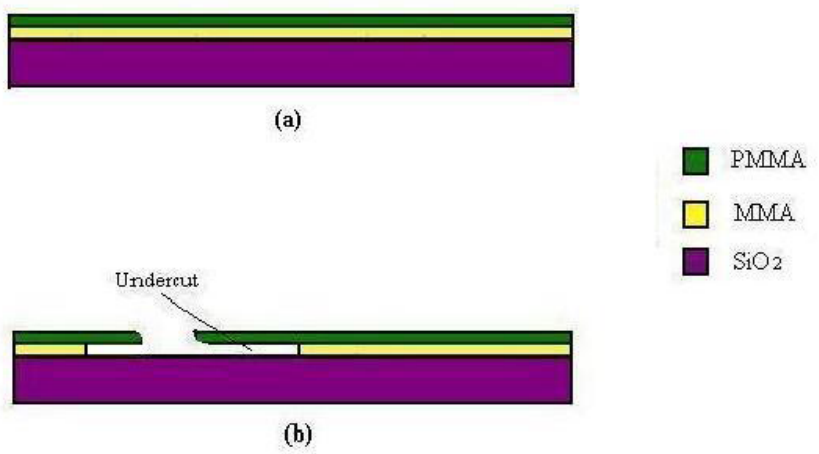

Figure 3.1: (a) Silicon wafer with double-layer polymer spin coating. (b) Diagram showing the undercut.

Procedures to make this double layer coating film are described here. Clean the silicon wafer by blowing dry nitrogen gas to remove dust, and then spraying acetone first and then isopropanol to the surface of the wafer while it is spinning at a speed of 5400 *rpm* to remove grease and some organic impurities. The spinner will stop after 60 seconds with the wafer surface clean and dry. Then put several drops of MMA solution at the center of the wafer and start the spinner to spin the bottom layer MMA at a speed of 1500 *rpm* for 90 seconds

to let the coating spread uniformly. Bake it on a hot plate at $150°C$ for 10 minute to dry. Then take the wafer back onto the spinner and spin the top layer PMMA at a speed of 5400 rpm for 60 seconds and bake it at $180°C$ for 10 minutes. Now, the wafer can be manually cut by a diamond pen into small pieces ,8 $mm * 8$ mm or so, as desired.

3.2 Electron-Beam Lithography

Electron-beam lithography(EBL) is a lithographic process which makes use of a focused beam of electrons to produce sub-micron patterns on e-beam resist coated substrates. Compared with optical lithography, which uses light for the same purpose, e-beam lithography has a higher resolution due to the smaller wave length possessed by high energy electrons. Resolution is the smallest detail that can be distinguished in an image. The minimum separation d that can be resolved by any microscope is calculated by the following formula:

$$d = \frac{\lambda}{2n \sin \theta} \tag{3.1}$$

where λ is the wavelength, n is the refractive index with $n = 1$ in vacuum. Resolution is inversely proportional to d and so to λ. Consequently, to achieve a higher resolution, we need to use a shorter wavelength. However, resolution can be constrained by other factors, such as electron scattering and back scattering. The excitation voltage of our scanning electron microscope (SEM) can be as high as 30 KV. Under this high voltage, electrons are drawn out of the filament, they pass through a series of electromagnets which act like lenses in optical microscopes and then become a focused beam with very small diameter. They can be scanned over the resist wafer without using masks as in optical lithography. On the other hand, electron beam produces patterns in serial, so it has a much smaller throughput than optical lithography which works in a parallel mode. While SEM is used, samples and filament are in vacuum. The vacuum environment is required because if the filament were surrounded by air, it would burn out quickly, just like a light bulb. Besides, if the sample chamber were in atmosphere, the electrons would collide with the gas molecules and never reach the sample, and the gas molecules could even contaminate samples.

We use the software DesignCAD LT 2000 to design patterns. Our pattern is shown in figure 3.2. It is composed of three layers. If we need to use different parameters for

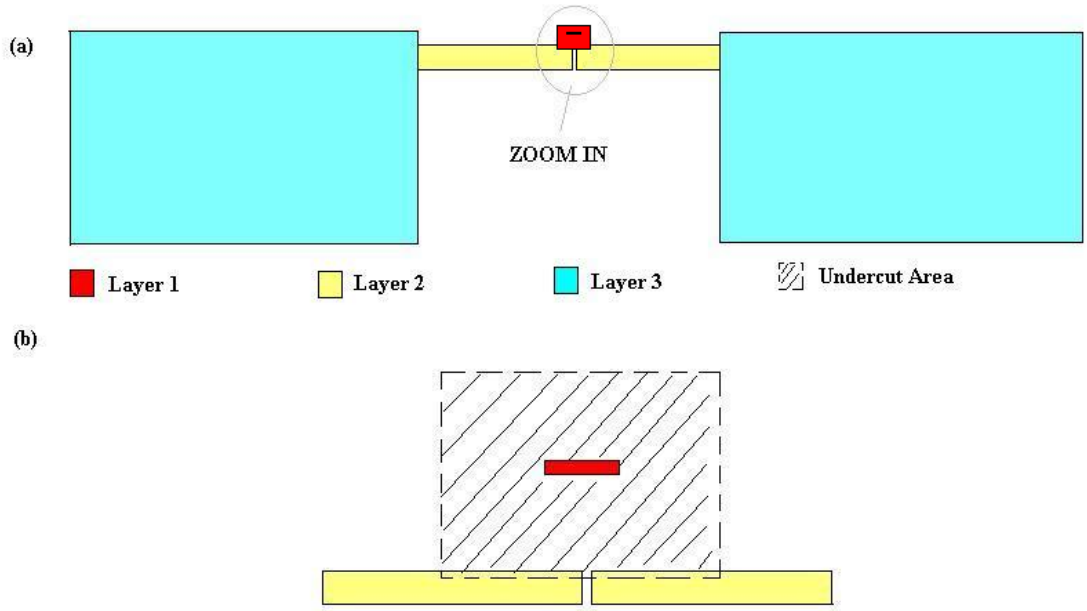

Figure 3.2: Pattern designed in DesignCAD: (a) Overview of the pattern, which contains three layers. (b) Zoomed in under cut part.

different elements in the same layer, we can assign them different colors. Once the pattern is designed, we generate the "run file" which contains the exposure conditions and alignment information for each pattern elements in Nanometer Pattern Generation System(NPGS), a popular SEM based lithography system. Using a run file is one advantage of NPGS that separates the pattern design from detailed exposure conditions. Consequently, we can draw the same pattern with different exposure conditions just by changing parameters in the run files. Exposure conditions include drawing electron beam current, electron beam dose, magnification, and center to center spacing. Once a run file has been created, the pattern may be written using the program NPGS. Generally, we use 30 KV excitation voltage to generate the electron beam. And for fine structures, high magnifications and small drawing currents are better for getting a higher resolution. Specifically for our sample, we use the following parameters. Layer 1 has the highest resolution. It contains a 200 nm long wire and an undercut. We use magnification 1000 and current 10 pA, line dose 2.25 nC/cm for the line structure, and area dose 125 $\mu C/cm^2$ for the undercut area. For layer 2, we use magnification 1000, drawing current 100 pA, and area dose 290 $\mu C/cm^2$. And for layer 3,

which is the biggest part in our pattern, the contact pad, we use magnification 60, current 6 nA, and area dose 475 $\mu C/cm^2$. The large current helps to expedite the drawing process when we don't need very high resolution of big elements like the contact pads. These doses are carefully selected after analyzing a series of testing samples. Appropriate dose selection is very important to avoid over dose and under dose. Over dose will destroy the pattern by causing connections at undesired positions or ruining the undercut. Under dose will give us a bad deposited metal film quality because the polymer is not totally removed.

When the lithography is done, we turn of the filament, vent the SEM chamber and take out our samples. Then we immerse these samples into the development solution to get rid of the exposed resist film, thus we get the pattern we want. The development solution is a mix of methyl iso-butylketone(MIBK) and isopropanol(IPA). The mixing ratio is 1:3 in volume. The development time is 35 seconds in our case. Then we wash them with IPA and blow them dry with compressed nitrogen gas. Finally, we check these samples under an optical microscope to confirm that they have the right pattern and are ready for evaporation.

3.3 High Vacuum Shadow Evaporation

High vacuum thermal evaporation is one of the physical vapor deposition (PVD) methods. It is frequently used to deposit thin films onto various surfaces. High vacuum is a desired environment to produce high quality films. In the pressure of 10^{-6} *torr*, it takes 1 *sec* to form a monolayer of the residual gases, which may contaminate samples. But at an even lower pressure, 10^{-8} *torr*, it takes 100 *sec* to form a monolayer, which is 100 times slower. Thus samples made at higher vacuum usually have higher purity and quality.

Our thermal evaporator is equipped with a cryopump. It utilizes very low temperatures to condense gases and thus trap them on its cold surface and thus get the base pressure about 10^{-8} *torr*. The temperature of its cold surface is below 20 K. This low temperature is achieved by the refrigerator connected to it. The refrigerator operates on the cycle which utilizes high-pressure helium gas from the compressor and expand it to produce cryogenic temperatures at the pump arrays. The heat produced by the compressor is cooled by a water chiller. Since the helium cycle is closed, the cryopump does not consume helium gas.

There is a crossover pressure for each cryopump, and for ours , the crossover pressure is between 0.1-0.2 *mbar*. We use the oil-sealed mechanical pump as the roughing pump to get down to the crossover pressure before we can connect the cryopump with the vacuum chamber by opening the high vacuum valve. The crossover point is crucial because it is where the cryopump must take all the pumping task without overloading. On the other hand, as the roughing pressure is getting lower, the backstreaming of oil vapor will increase and those entering the vacuum chamber can have detrimental effects on most processes and finally reside in the charcoal layer of the cryopump, which leads to a replacement of the charcoal layer sooner or later. Cryopump need to be regenerated every few months to release the trapped gases on the charcoal layer thus recover its full ability to achieve very low base pressure.

The thermal evaporator uses electric current to heat the source material over its melting point, raise its vapor up, and deposit the vapor material onto the substrate above the source. This procedure is done in the high vacuum chamber, with base pressure as low as $10^{-8} torr$. Such high vacuum allows the source material vapor to reach the substrate without interacting with any other gas-phase atoms inside the chamber.

The sample is ready to be put into the high vacuum thermal evaporator chamber after we check it under an optical microscope to make sure we have the desired pattern on it. The sample is attached onto a rotary stage by a tiny piece of tape. The nanowire pattern need to be aligned to the rotation axis of the stage, otherwise, the shadow evaporation will give us poor or even unusable samples. The rotating angle can be set by two stopping screws(see Figure 3.3). We can rotate the stage without breaking the vacuum. The thickness of deposited metal film is measured by a crystal monitor, and we start and stop the deposition by opening and closing the shutter inside the chamber.

After loading the sample stage and source materials in to the evaporator, we start to pump the chamber with a mechanical pump first to reach the roughing pressure between 0.1-0.2 *mbar*, then we close the mechanical pump and open the high vacuum valve to continue to pump the chamber with the cryopump. When the pressure reaches 10^{-7} *torr* range, we can start the deposition procedures. At first, the rotating stage is horizontal, thus the metal is

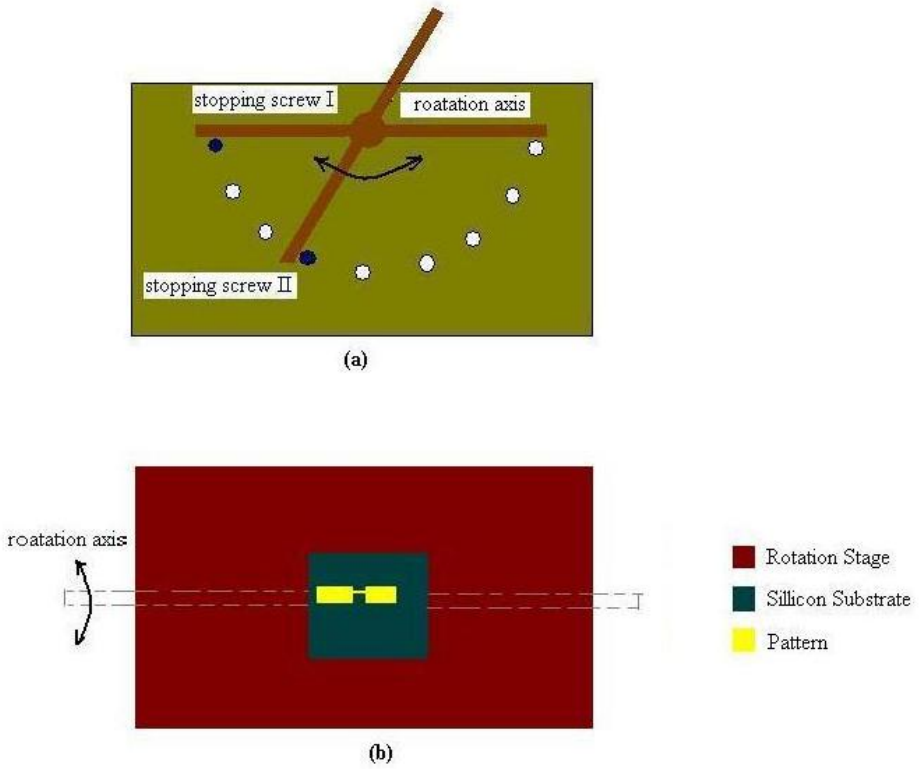

Figure 3.3: Diagram of our rotating stage designed for shadow evaporation. (a) Side view: horizontal and tilted positions controlled by two stopping screws. (b) Top view: sample is exaggerated to show alignment.

deposited vertically on to the sample surface. Cobalt (Co) is the first layer. The deposition rate is 0.5 nm/sec. When the Co thickness reaches 10 nm, we stop the deposition by closing the shutter and turning off the melting current. Then we rotate the stage until it is stopped by the other stopping screw, where there is the appropriate angle chosen carefully between the stage surface and the metal evaporation direction. Now we deposit the seconde layer copper (Cu) at the rate of 0.5 nm/sec until the thickness reaches 100 nm.

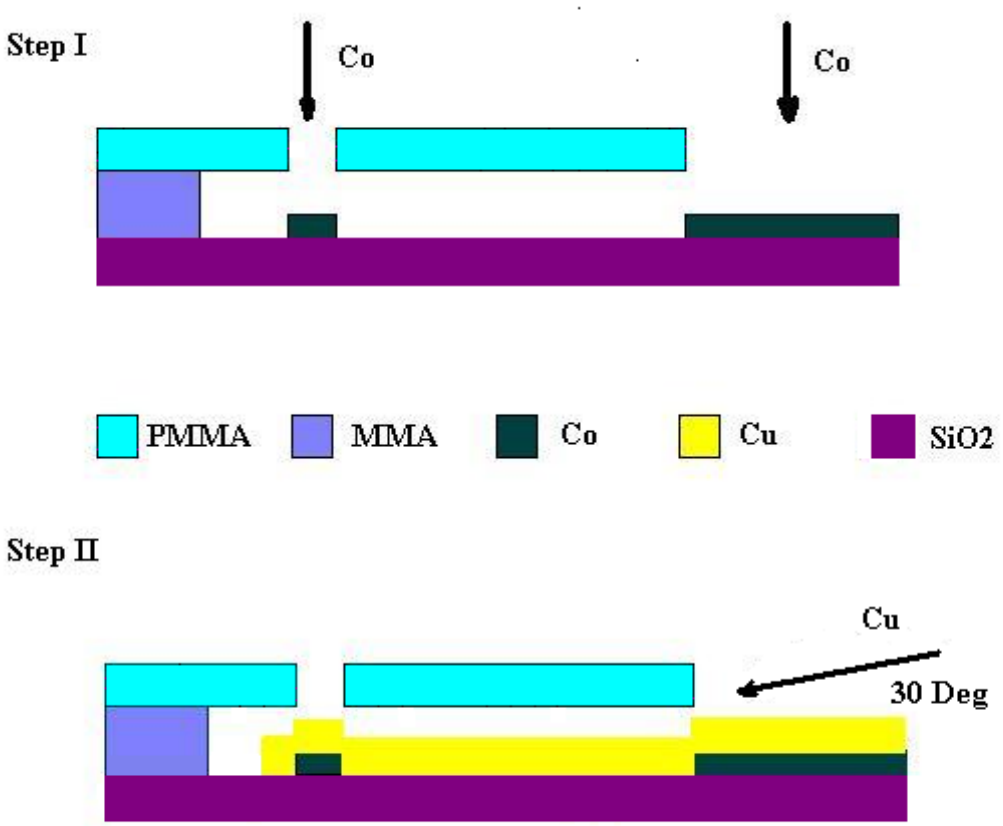

Figure 3.4: Two deposition steps. Step I: deposit Co layer vertically .Step II: deposit Cu layer with 30 degrees shadow evaporation

The interface between Co and Cu is nearly free from adsorbates because the Co surface is exposed to base pressure for less than 10 seconds. The Co nanoparticle is 1.5 μm away from the other Co area to remove the influence of stray magnetic field from other magnetic parts of the sample. After about 15 minutes, the temperature inside the evaporation chamber

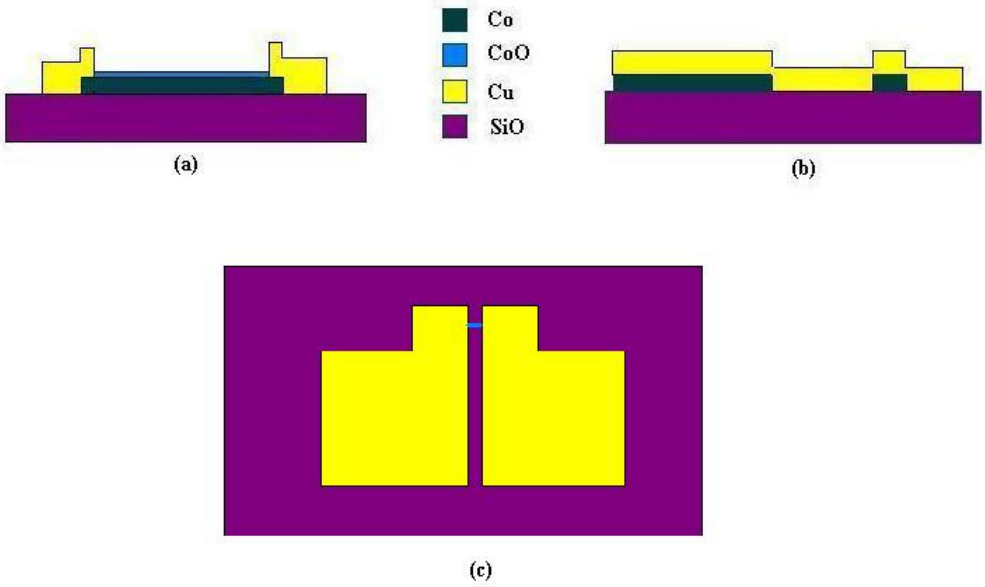

Figure 3.5: Diagram of our sample made by shadow evaporation technique. (a) End view cross section: exposed Co is surface oxidized to CoO (b) Side view cross section: Co nanoparticle is away from other Co area (c) top view

drops back to room temperature. We then disconnect the cryopump with the chamber by closing the high vacuum valve and then we vent the chamber to atmosphere. We take out the sample and immerse it in acetone for 10 minutes. The metal film deposited on the unexposed resist is dissolved in acetone and thus removed together with the resist. However, the metal deposited directly onto the silicon wafer survives. Next, we rinse acetone off the sample with isopropanol and blow it dry with compressed nitrogen gas. Consequently, we have the designed pattern left. The sample is now exposed to air and will be transferred to a dilution refrigerator. Exposure to air induces surface oxidation of uncovered cobalt and generates a layer of cobalt-oxide(CoO), which covers the Co film. The time of air exposure before evacuation in the dilution refrigerator is about 1 hour.

To characterize the CoO thickness, we measure the resistance of Co films with various thicknesses *in situ* and monitor how the resistance increases when the films are exposed to air for 1 hour. From this we infer that the thickness of Co metal is reduced by approximately 2nm after 1 hour of air exposure. A typical sample is shown in Figure 3.6.

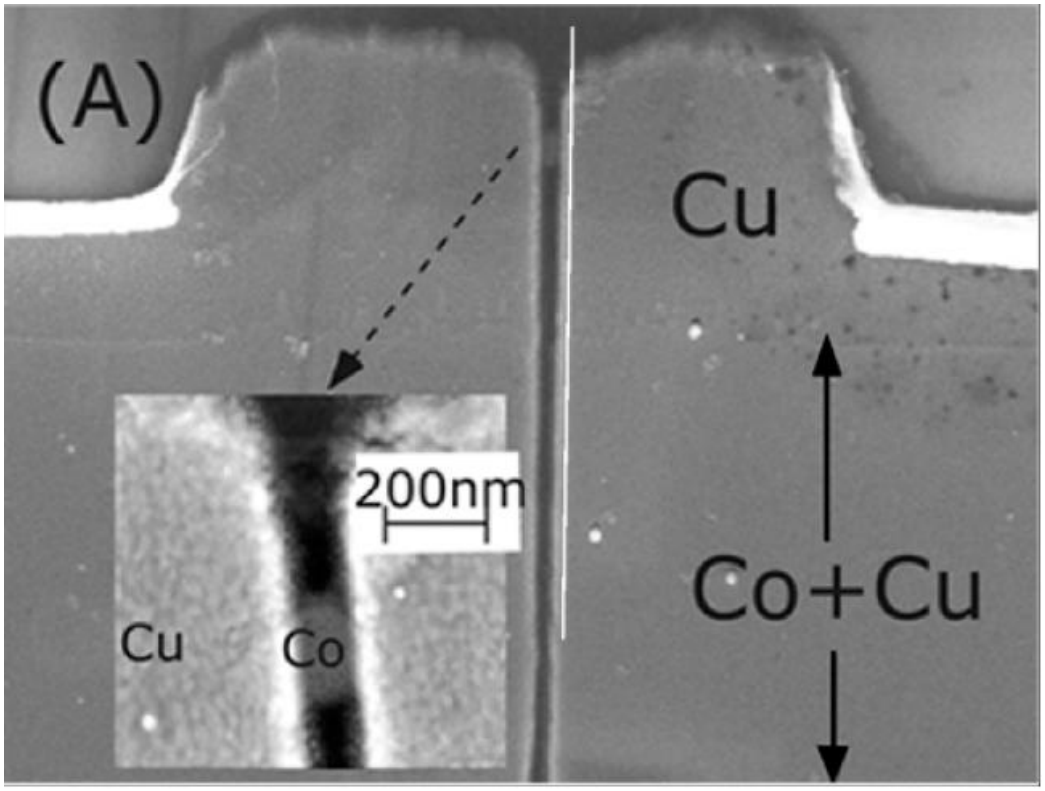

Figure 3.6: SEM image of a typical sample, the insert is the zoom in of the Co nanoparticle arar. The Co nanoparticle is of 200 nm diameter and 10 nm thickness in contact with two Cu lead of 50 nm thickness. The gap between Cu leads is 100 nm.

CHAPTER IV

EXPERIMENTAL TECHNIQUES AND MEASUREMENTS

4.1 Low temperature Measurements in Dilution Fridge

A dilution refrigerator is an essential equipment to do low temperature experiments. It can provide and retain a temperature as low as 15 mK, which fulfills our mesoscopic experimental requirements. In 1951, Heinz London proposed its principle of operation. Dilution fridge uses a mixture of two isotopes of helium (^3He and ^4He). The mixture will be separated into two phases spontaneously when it is cooled below a critical temperature below 700 mK. The two phases are respectively the condensation phase which is lighter and rich in ^3He and the dilute phase which is heavier and rich in ^4He. Due to the difference between the enthalpy of ^3He in these two phases, it is possible to evaporate ^3He from the condensation phase into the dilute phase and consequently cool the system. The concentration of ^3He is less than 6% in the dilute phase even when the temperature approaches absolute zero, so this evaporation process continues to work at extremely low temperatures.

Our dilution fridge is equipped with a superconducting magnet. It is immersed in the liquid helium bath while in use. Superconducting magnet provides a more stable magnetic field in general and consumes much less power, especially in the persistent mode. To generate a sweeping field, we need to let the persistent switch on. The persistent switch is consist of an internal heater and a short segment of superconducting wire connected across the input terminals of the magnet. When the heater is on, it heats the short wire into normal state, i.e, the wire becomes resistive. So a DC voltage can be established across the wire as well as the terminals of the magnet. Then the magnetic field will sweep as the voltage sweeps. The superconducting magnet equipped in our cryostat can provide the magnetic field as big as 14 T. It is controlled by an operating system. It can sweep

to a preset magnetic field at a selected rate automatically. The generated magnetic field direction is along the axis of the cylindric cryostat, i.e. perpendicular to the horizontal ground. The whole system is put in a electromagnetically shielded room such that our samples are prevented from some undesired external radiation.

We mount the sample on a sample holder using ultra thin non-insulated copper wires to connect the sample electrodes to the pins of the sample holder. Indium dots are easily used to stick copper wires onto the surface of contact pads. Now the sample (mounted on the sample holder) can be transferred into the dilution fridge. Since there is a 4.2 KΩ filter in the fridge in series with the sample, and our sample resistance is typically in the 100 Ω - 200 Ω range, we have to employ the four-probe measurement to extract the sample resistance. This technique is widely used to remove spurious downstream anomalies such as contact resistances [6].

After the sample is loaded, we bake the sorb for 30 seconds with a heat gun and then close the fridge inner vacuum chamber (IVC) with indium seal. Pump the IVC, still, 1K pot and condenser to vacuum with a turbo pump and do the leak check with the Heliot leak detector by spraying tiny helium gas flow all over the IVC. When the system is confirmed to be reliable, we load it into the cryostat and assemble the system properly. Put 5 mm^3 helium exchange gas into the IVC, which will provide necessary heat exchange during the cool down. At 4.2 K, the helium gas in the IVC need to be pumped by the sorb before we start condensation.

Pump all the lines into vacuum and do a leak check for them. Then transfer liquid nitrogen into the cryostat to pre-cool the system to 77 K. Leave liquid nitrogen in the cryostat overnight, blow it completely out of the cryostat with helium gas the next day. Then transfer liquid helium into the cryostat. With the cryostat filled with liquid helium, we can do some 4.2 K measurements, such as taking several AMR curves to identify good samples. To go down to base temperatures, we need to run the fridge by condensing the mixture and then circulating the mixture.

4.2 Four Probe Measurement Technique

Four probe measurement, just as its name implies, employs four probes. Two are used to inject and sink current, the other two are used as voltage taps. A schematic diagram is shown in figure 4.1. The sample resistance is calculated as [6]:

$$R = \frac{V_2 - V_3}{I_{1\to 4}} \tag{4.1}$$

If we simply use two probes to measure a sample resistance, we actually also measure the contact resistance. In those cases that the sample resistance is very small, the contact resistance will dominate and thus obscure changes of the sample resistance itself. The effect of contact resistance can be eliminated by using four-probe measurement. In our experiment, although our sample resistance is not very small, it is behind a 4.2 KΩ RF-filter. So we have to employ four-probe measurement, otherwise, we will measure the voltage across the sample together with the filter. Our sample resistance is much smaller than 4.2 KΩ, then the filter will obscure changes of the sample resistance.

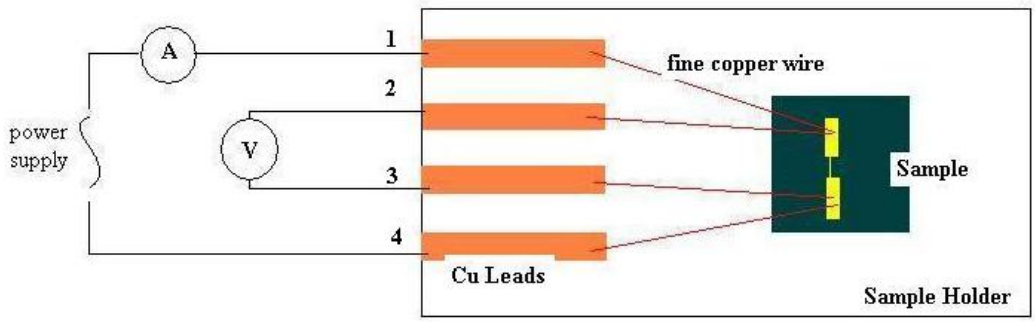

Figure 4.1: Diagram of sample mounting with a four-probe setup. Leads 1 and 4 serve as current probes, leads 2 and 3 serve as voltage probes.

4.3 Experimental Setup and Data Acquisition

The schematic diagram of our measurement circuit setup is shown in fig 4.2. We use a lock-in amplifier to provide a sinusoidal AC voltage with 233 Hz frequency and a signal generator to provide a triangular voltage with 0.0015 Hz. The triangular voltage has a much less frequency than the sinusoidal voltage. So the triangular voltage acts like a slowly varying DC voltage. Our sample is connected in serial with a much bigger resistor of 100

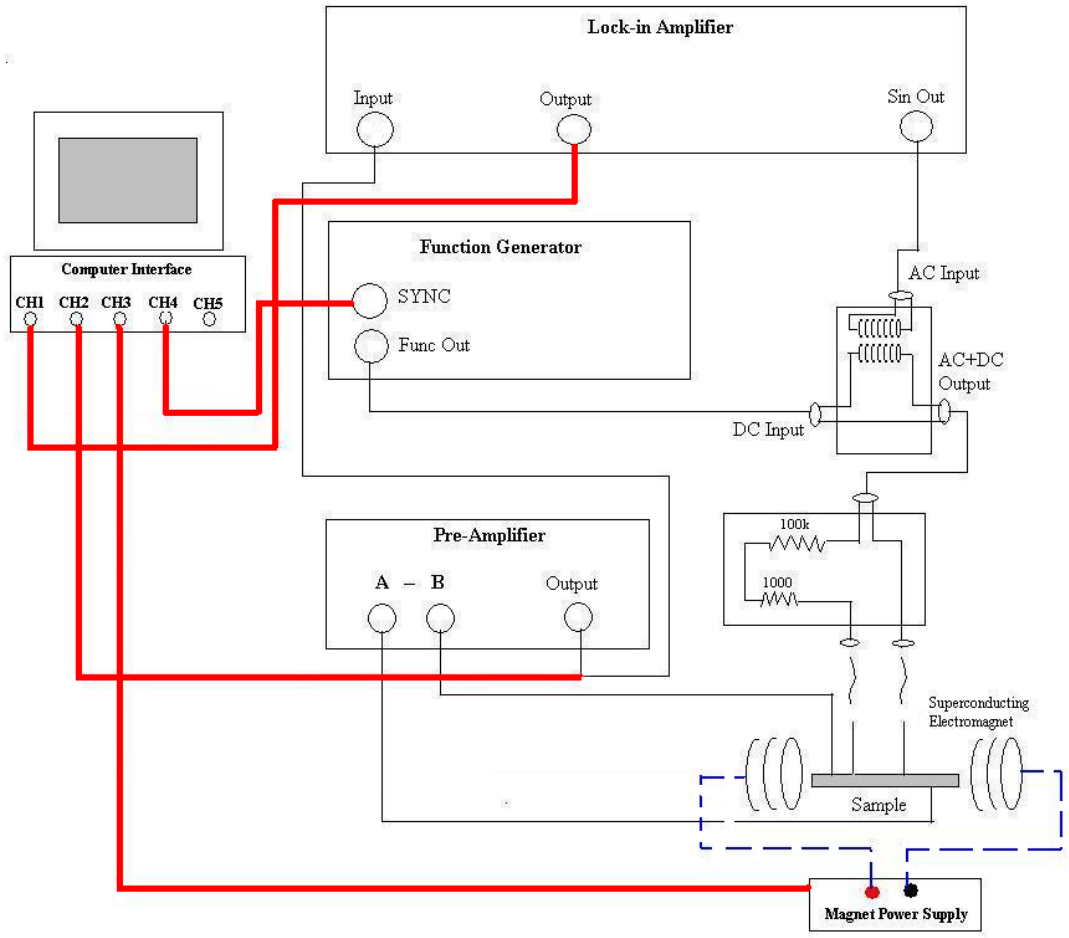

Figure 4.2: Schematic diagram of measurement setup: solid lines represent electrical connections; dashed lines represent a separate circuit controlling the superconducting magnet; bold solid lines represent data transmission cables to the computer interface.

KΩ. Since we employ the four-probe measurement, there are 4 terminals of a sample. Two are the current terminals, the other two are voltage terminals. From the voltage terminals,

the voltage across the sample is sent into a pre-amplifier, and is amplified 10 times; amplifier output is connected to the input of the lock-in amplifier, so we can read this voltage on the lock-in amplifier. We collect all the data with a computer through LabView software. Since our sample resistance is between 100 Ω and 200 Ω, which is very small compared with 100 KΩ, the current flowing through the circuit is approximately equal to the overall voltage divided by 100 KΩ. To study the magnetoresistance, we also need a magnetic field in our experiment. The superconducting electromagnet is the provider of the magnetic field and is controlled by a separate circuit.

CHAPTER V

MESOSCOPIC RESISTANCE FLUCTUATIONS IN COBALT NANOPARTICLES

During the past two decades, as the technique to fabricate smaller samples developed and the ability to do experiments at extremely low temperatures improved, many new phenomena have been observed experimentally. These phenomena cannot be explained by the ensemble-averaging approach used in bulk systems. Although these samples are much bigger than atomic dimensions, the macroscopic approach breaks down. A new field of mesoscopic physics emerges. In this regime, the transport electrons can no longer be treated as particle diffusion. People have to use wave mechanics approach to describe their behaviors. In micron scale metallic samples at low temperatures, interference among scattered electron waves creates noticeable contributions to sample resistance, including random but reproducible fluctuations in conductance [6, 58, 59]. One remarkable consequence is that the resistance of phase-coherent samples becomes sensitive to microscopic impurity configurations.

Mesoscopic effects in ferromagnets could be different from mesoscopic effects in normal metals [60, 1, 2, 3]. In macroscopic normal metals, magneto-resistance (MR) can be observed only if

$$\omega_C > f_e, \tag{5.1}$$

where, $\omega_C = \frac{eB}{m}$ and $f_e = \frac{v_F}{l}$ is the electron scattering rate. When the magnetic field B is as big as 10 T, the mean free path l need to be as long as 1 μm. Thus normal metals have to be very clean to see magneto-resistance, and those with a short mean-free path do not exhibit classical magneto-resistance. But in ferromagnets, magneto-resistance is possible even if $\omega_C << f_e$. Thus weakly disordered ferromagnets with a similar mean-free-path can display magneto-resistance, which includes domain wall resistance (DWR)[5, 30, 31, 61, 32,

34, 62, 33, 63, 64, 65] and anisotropic magneto-resistance (AMR)[4]. Magneto-resistance could lead to novel mesoscopic electron effects because the wavefunction phase depends on the scattering potential and interference among the scattered electron waves depends on the phase shift [2, 3]. Signatures of mesoscopic electron transport in ferromagnets have been reported prior to our work. [10, 11, 12, 13]. However, the dependence of the phase of the electron wave function on magnetization-reversal processes have not been measured yet.

In this experiment, we investigate the resistance of mesoscopic ferromagnets cobalt(Co) at low temperatures and find that the resistance is very sensitive to the magnetic state of the sample. In particular, we observe significant wave-function phase shifts and attribute those to domain walls. We study how the fluctuations respond to magnetization-reversal processes with bias voltage, bias fingerprints.

5.1 IP and OP Magneto-resistance

Our data is taken in two different directions. One is out-of-plane(OP, magnetic field perpendicular to the Co film plane, and thus to the current) and the other is in-plane(IP, magnetic field parallel to the Co film plane but still perpendicular to the current). Differential resistance is

$$r = dV/dI. \tag{5.2}$$

It is recorded by the lock-in amplifier while the magnetic field is sweeping between -2.4T and 2.4T at temperature T = 6K. The magnetic field is initially set to -12T to polarize CoO as much as possible, then it is reduced to the starting point -2.4T. Figure 4.2 gives the measurement circuit setup diagram. The applied current on the sample is

$$I_{AC} = i\cos(2\pi f t), \tag{5.3}$$

where $i = 0.5$ μA, and $f = 80$ Hz.

Since CoO is antiferromagnetic, The Co/CoO interface generates an exchange-bias effect (See figure 5.1) in Co [64, 66, 67], which leads to pinning of the magnetization and the enhancement of the coercive field. It's harder to reverse the spins in exchange biased Co than in unbiased Co (under Cu). We expect that domain walls are nucleated at the

interface between the exposed Co and unexposed Co by applying well-defined magnetic fields, analogous to the similar behavior shown in [64]. The Co nanoparticle is big enough support domains because the domain wall width (δ_w) in Co is =15 nm [30, 31, 61], which is much smaller than the sample diameter.

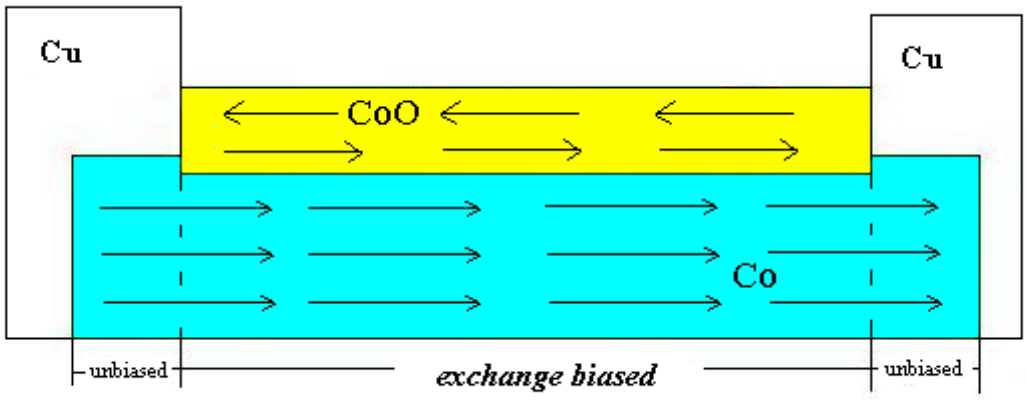

Figure 5.1: Exchange bias effect. Surface spins from CoO pin the spins in Co. It is harder to reverse spins in exchange biased Co than in unbiased Co.

The in-plane magneto-resistance data is taken at 6 K. In figure 5.2, the in-plane magneto-resistance curve shows a clear hysteresis. There are two sharp resistance transitions in each magnetic field scan direction. The lower transition indicates the nucleation of domains, while the high field transitions indicates annihilation of domains, respectively. The smaller coercive fields are symmetric , $B_C = \pm 62$ mT, which can be explained if the magnetization is first reversed in unexposed Co(under Cu). The spins in exchange biased Co have not been reversed yet at this small field due to the pinning effect of CoO/Co as expected. Thus, domains are generated in the nanoparticle. As the magnetic field continues to increase to some point, the magnetic moments in exchange biased Co change direction finally. Then the domain walls disappear. These are the larger coercive fields, 330 and -220 mT. The larger coercive fields in two different field direction are not symmetric, the coercive field is larger in magnitude when B increases. This is because magnetic field B is initially -12T. The resistance increases when the domains are nucleated.

The resistance increase at the smaller coercive fields is explained by the AMR inside

the domain wall, not DWR. As the unbiased Co reverses its magnetization while the biased Co has not at the smaller fields, two 180° Neel walls are formed. The angle between the magnetization inside the wall and the current is smaller than 90°, thus the sample resistance is increased due to the AMR effect in ferromagnets. DWR also contributes to the resistance increase but with much smaller magnitude compared to AMR.

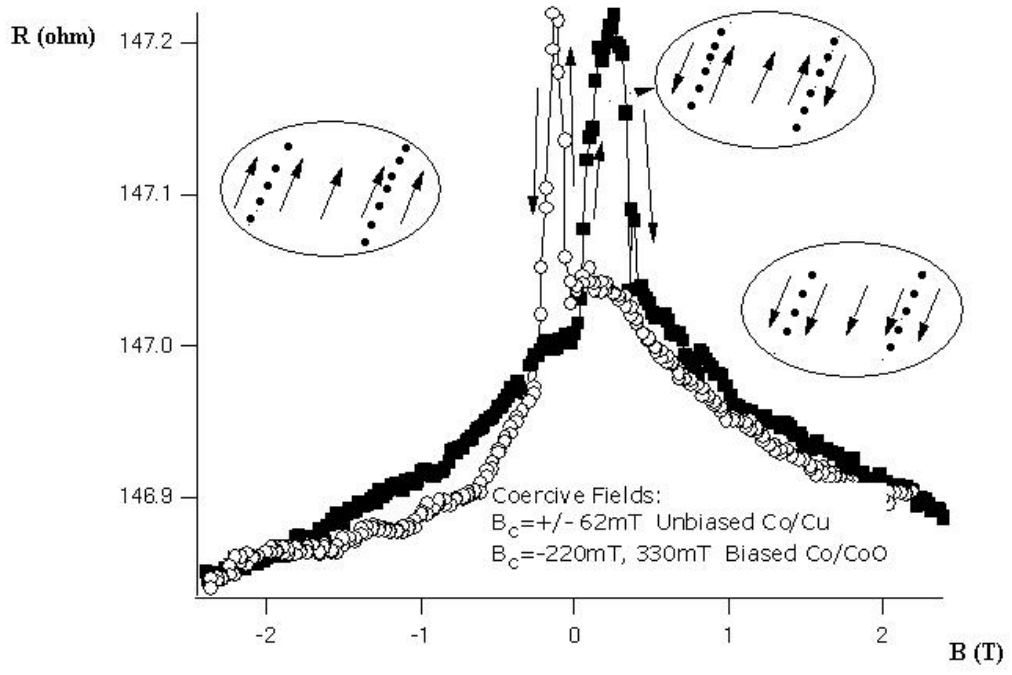

Figure 5.2: In-plane magneto-resistance. Set magnetic field initially at -12T to polarize CoO as much as possible, then reduce the field to -2.4 T and cycle between -2.4 T-2.4 T

Next we discuss the out-of-plane magneto-resistance (OP-MR) data. The graph is shown in figure 5.3. OP-MR exhibits a broad maximum at B=0 and a weak hysteresis. The maximum is explained as arising from the rotation of magnetic moments supported by the shape anisotropy. The easy axis of the nanoparticle is along the current direction. As the magnetic field decrease, the magnetic moments rotate from perpendicular to the film plane into the film plane to align with its easy axis, thus the angle between magnetic moments and the current is reduced, so r increases. This result is consistent to the anisotropic magnetoresistance of ferromagnetic materials, where $\rho_{\perp} < \rho_{//}$.

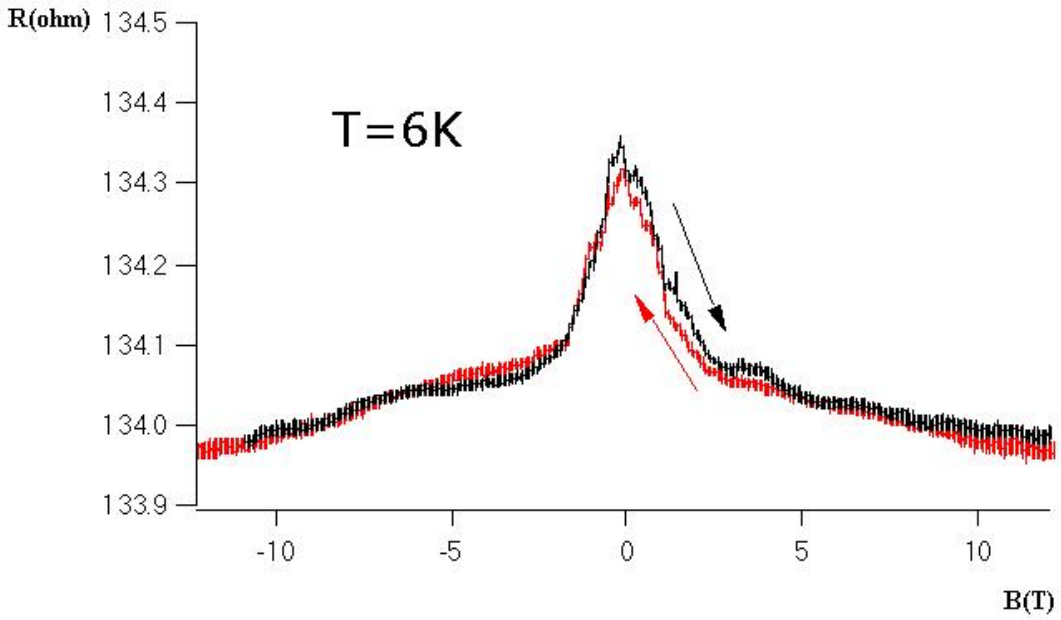

Figure 5.3: Out-of-plane magneto-resistance. It shows a continuous rotation of magnetic moments. Resistance is maximal when current and magnetization are parallel, and hysteresis is relatively weak.

5.2 Fluctuations in Differential Resistance

At T=0.03k, differential resistance

$$r = dV/dI \tag{5.4}$$

is measured as a function of both the dc-bias voltage V and the applied magnetic field B, i.e.

$$r = r(V, B). \tag{5.5}$$

The applied current is

$$I_{AC+DC} = I + i\cos(2\pi ft), \tag{5.6}$$

where $i = 0.5$ μA,and $f = 80$Hz.

Then , r is obtained by measuring the AC voltage across the sample with a lock-in amplifier. At $T = 0.03$ K, we confirm that *r(V,B)* is independent of i when $i < 0.5$ μA. The resistance of Cu leads is about 10 Ω and is not subtracted from r.

When the sample is cooled from 6 K to 0.03 K, the sample resistance increases by about

6 Ω. See the resistance comparison in figure 5.4, data are taken at 6 K, 3 K and 0.03 K. You can see a clear trend that the lower temperature, the higher resistance. Similar effect is reported in Co films at temperatures above 1.5 K [68] and is attributed to enhancement of electron-electron interactions caused by phase coherence [69].

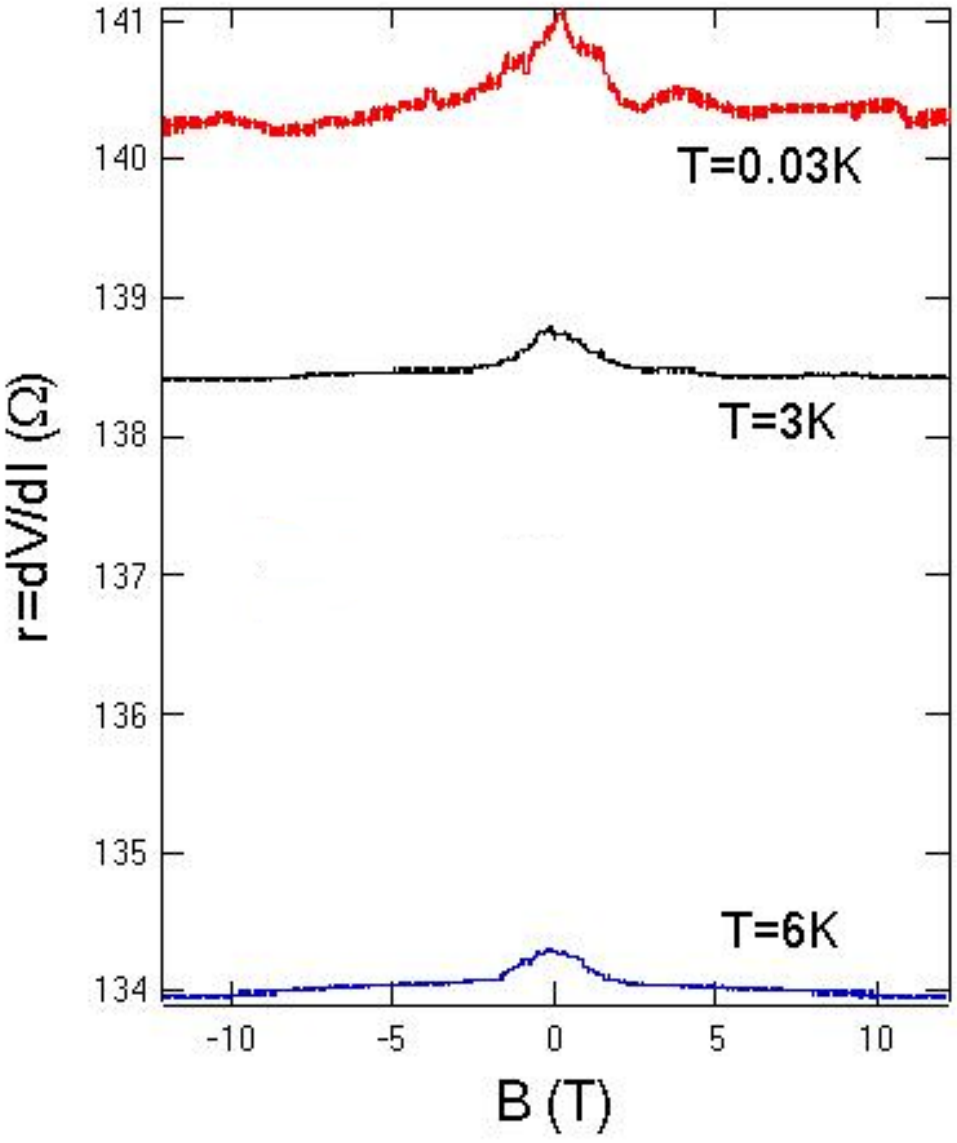

Figure 5.4: Electron-electron interaction effect (EE). Data are taken at 6 K, 3 K and 0.03 K respectively. The lower the temperature, the higher the resistance.

To study mesoscopic effects, we obtain the dependence of differential resistance r on two independent parameters, V and B, r *(V,B)*. The dependence is obtained by quickly sweeping

the bias voltage, while the applied magnetic field is slowly changing. Figure 5.5 displays *r(V,B)* when B is out-of-plane. Brighter pixels correspond to larger resistance. Thus, the white cross in this image displays maxima in resistance versus field and voltage, centered at zero field and zero voltage, respectively.

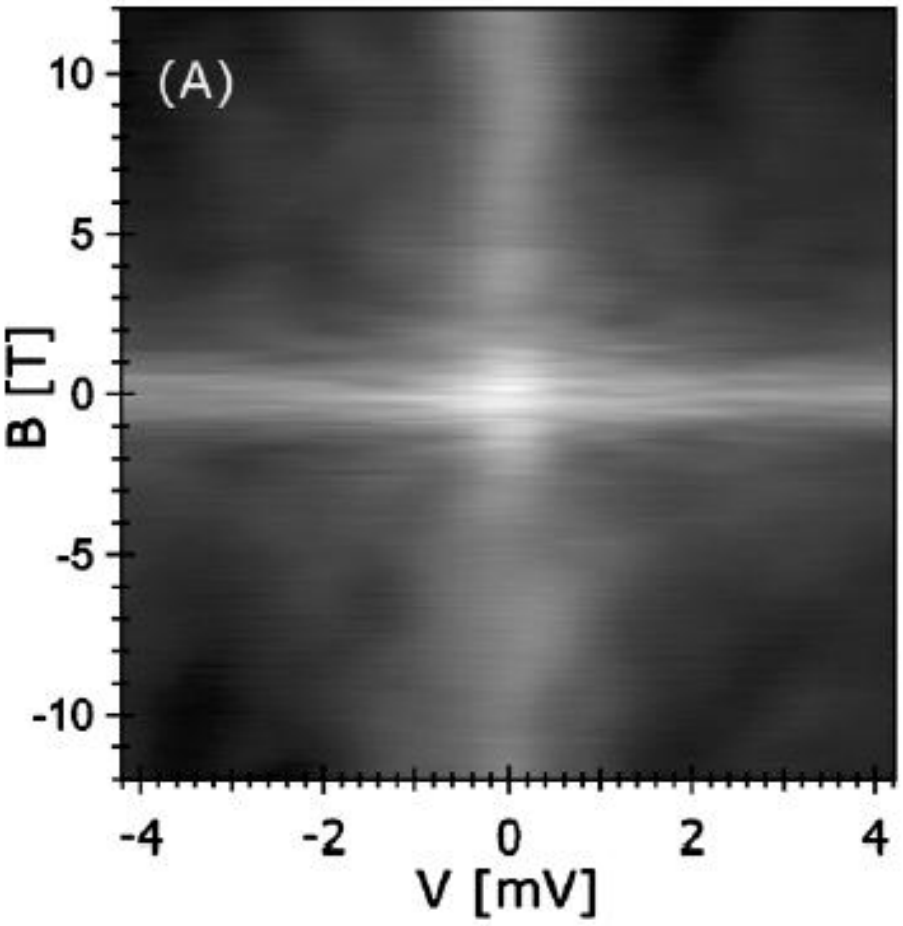

Figure 5.5: Differential resistance r versus bias DC voltage and out-of-plane magnetic field at 0.03 K. Brighter pixels represent larger resistances.

The average resistance versus field and voltage are defined as

$$r_0(B) = \int_{-V_{\max}}^{V_{\max}} r(V,B)dV/2V_{\max} \tag{5.7}$$

and

$$r_0(V) = \int_{-B_{\max}}^{V_{\max}} r(V,B)dB/2B_{\max} \tag{5.8}$$

respectively, where $B_{max} = 12$T, and $V_{max} = 4.2$ mV. The averages are shown in figures 5.7 (a) and 5.7 (b). The resistance averaged over both V and B is $r_0 = 140\ \Omega$. The average magnetoresistance (MR) at 0.03 K is enhanced compared to the AMR at 6 K (See figure 5.6). This enhancement suggests that weak localization effect contributes to magneto-resistance at low temperatures. Prior research in Co films did not find any weak localization effects at temperatures above 1.5 K [68]. Our temperatures are much lower than 1.5 K, which could explain the difference between the results.

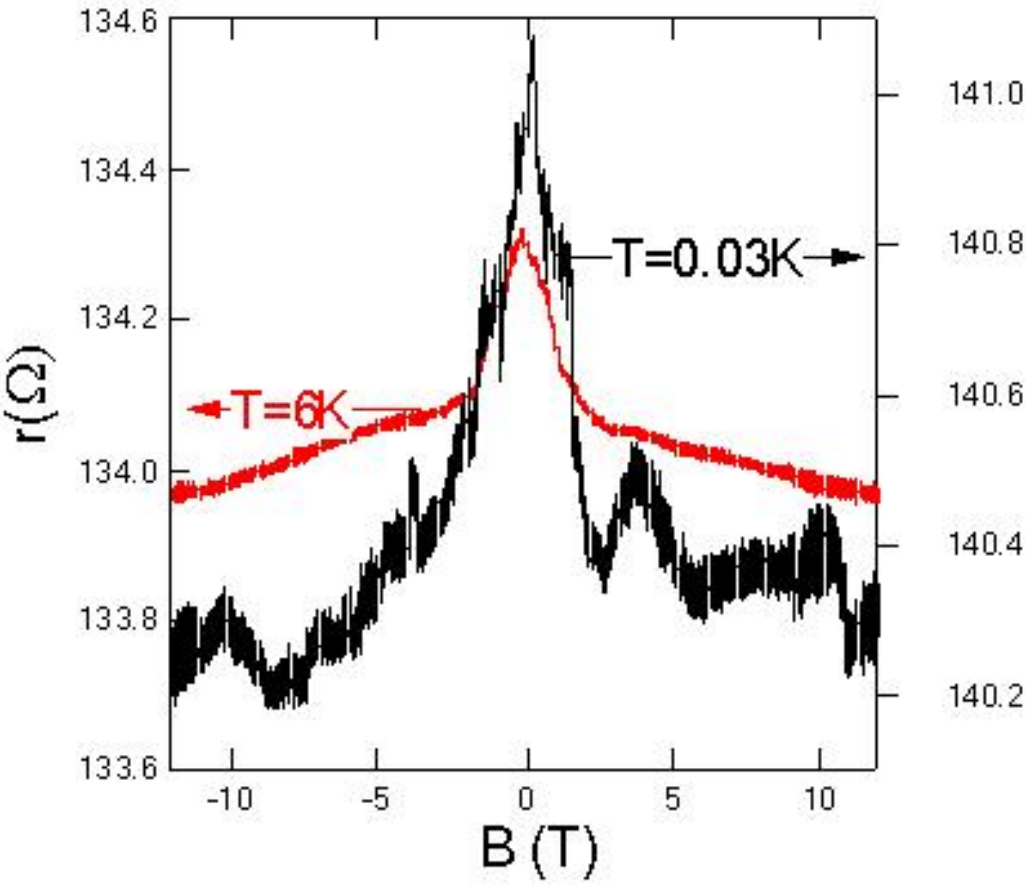

Figure 5.6: Average magnetoresistance is enhanced at 0.03 K compared to the AMR at 6K. This is due to the weak localization effect.

The weak localization magnetoresistance contribution cannot be extracted from data because of the internal field of Co. The total magnetic field acting on conduction electrons in Co cannot be equal to zero, instead, it is equal to the sum of the applied field and the internal field (1.8 T), which is much larger than the coercive fields. Thus, the low-field contributions to quantum interference effects, such as weak antilocalizaion, are experimentally inaccessible. So we are going to study conductance fluctuations (CF) only. The resistance

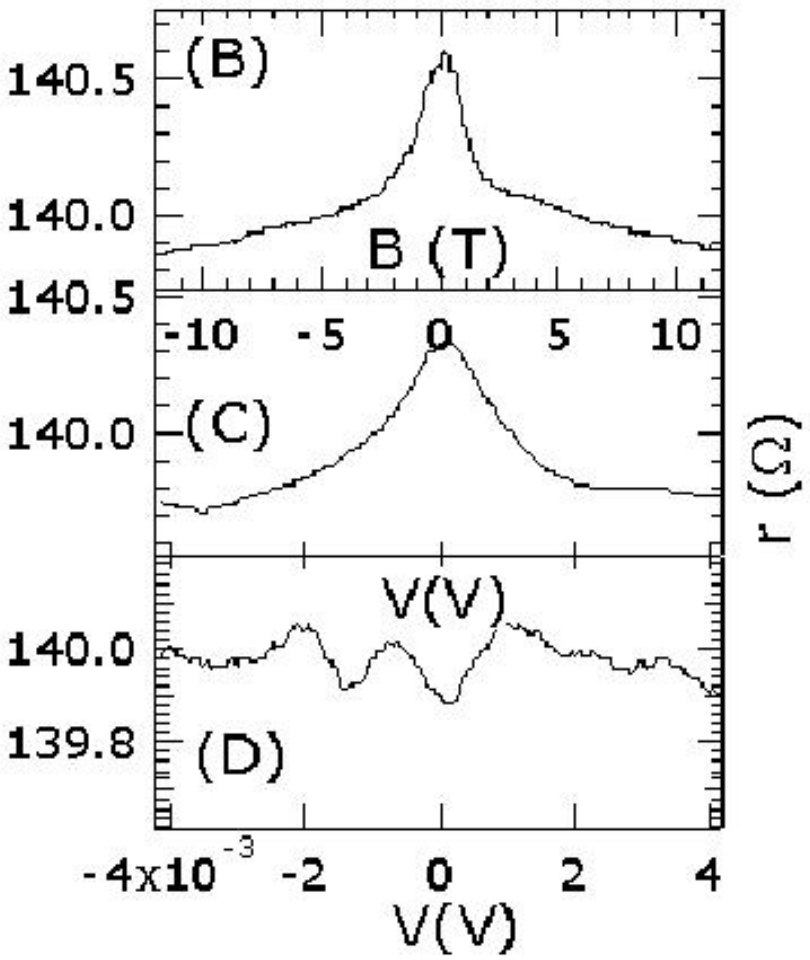

Figure 5.7: (a) Average resistance versus out-of-plane magnetic field. (b) Average resistance versus dc-bias voltage. (c) Fluctuations in resistance with de-bias voltage, $r(V,B) - r_0(V) + r_0$, at B = -5.5 T

maximum with voltage in figure 5.7 (b) is a consequence of the electron-electron interaction

enhancement effect (EE) in mesoscopic samples [70]. Resistance fluctuations in figure 5.5 are superimposed with the EE effect and the AMR. In other words, conductance fluctuations are obscured by the EE effect and AMR (white cross in figure 5.5). To display the pure fluctuations, we subtract the white cross in 5.5, which is the average resistance versus field and average resistance versus bias voltage. Then we get figure 5.8 which shows the fluctuations clearly. To better display the fluctuations in resistance with voltage, we need to extract the conductance fluctuations from the superimposed data. We find the difference between $r(V,B)$ and the average EE effect in figure 5.7(b). The resulting resistance as a function of voltage at fixed magnetic field is shown in figure 5.7 (c). The resistance now clearly exhibits fluctuations with DC bias voltage. The fluctuations are reproducible and are found at base temperatures only.

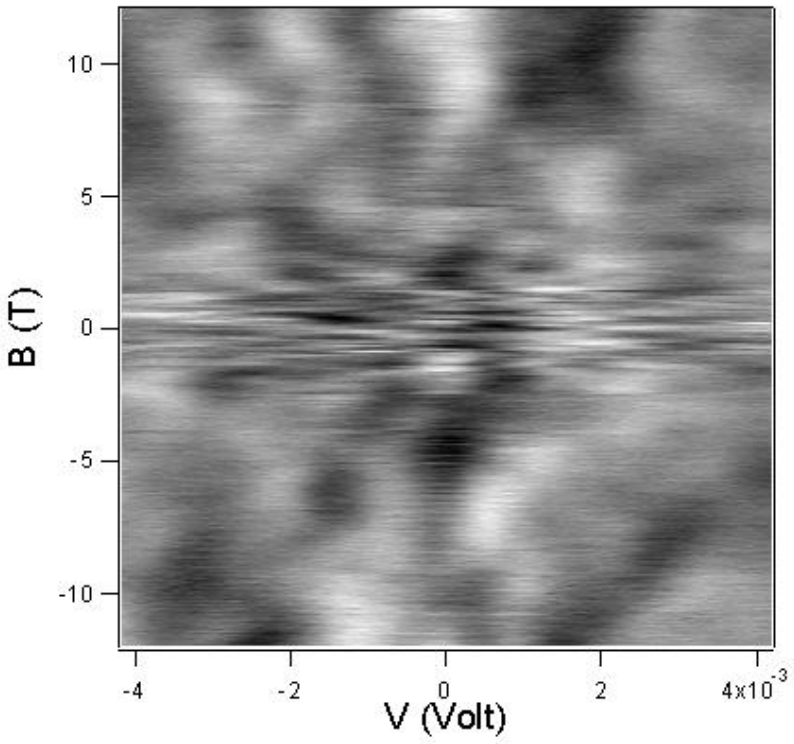

Figure 5.8: Resistance fluctuations versus magnetic field and dc-bias voltage.

The fluctuations in r with V represent changes in electron interference from constructive

to destructive as a function of electron energy [6]. Root-mean square (rms) of the fluctuations is 0.1 Ω, which corresponds to rms-CF of $0.05e^2/h$. The fluctuation amplitude is much smaller than e^2/h, showing that the dephasing time must be much shorter than the transport time. The rms dose not change with V, showing that the heating effects are weak.

The correlation voltage V_C is given by the average spacing between minima and maxima, $V_C \approx 0.5$ mV. The meaning of V_C is that changing the electron energy by eV_C changes the electron phase at a typical phase-coherent electron trajectory by π. V_C is related to the dephasing time τ_ϕ as [38]

$$|e|\ V_C = \hbar/\tau_\phi, \tag{5.9}$$

so

$$\tau_\varphi = \frac{h}{|e|\,V_C} = 1.3ps. \tag{5.10}$$

5.3 Discussion of the Results

To display the fluctuating part of the resistance, we subtract the average EE effect and MR from the resistance. Four red-white-blue scale images in figure 5.9 display conductance fluctuations with magnetic field and bias voltage at 0.03 K refrigerator temperature. Red and blue regions indicate larger and smaller resistance, respectively.

The fluctuations with field and voltage, represented in figure 5.9, are not reproducible when the field is varied arbitrarily. However, the fluctuations are reproducible when B varies between two fields in the same direction after an initial training with one field cycle.

Compare the fluctuations in differential resistance in weak field as shown in figure 5.9(A) and 5.9(B), we find there is a noticeable difference between dependence of the bias fingerprints on the IP (in plane) and the OP (out of plane) fields. If the IP field varies from -2 T to 0, the resistance maxima and minima with voltage shift weakly. By contrast, when B is changing OP, bias fingerprints shift or rearrange several times. These rearrangements are indicated by the bright and dark regions along the field direction. This indicates the wave-function phase is magnetization dependent.

For the IP fingerprints under large field range (-12 to 12T), figure 5.9(C) shows that

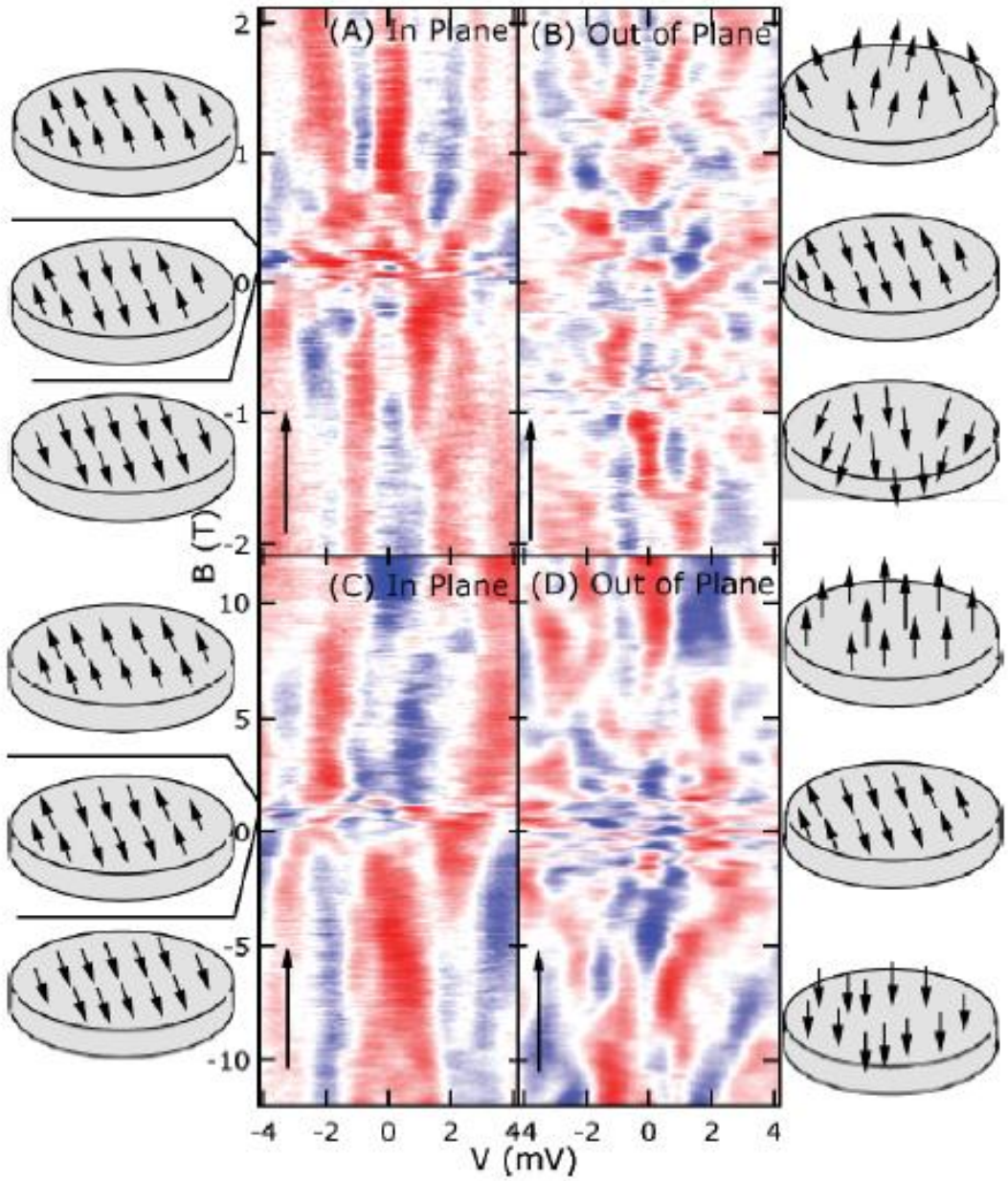

Figure 5.9: (A),(B) Fluctuations in differential resistance in weak field, $r(V,B) - r_0(V) - r_0(B)$,with V and the in-plan field and the out-of-plan field, respectively. (C),(D) Fluctuations in differential resistance in strong field.

bias fingerprints vary weakly with the IP field in the field range -12 T $< B <$ 0. But, when the IP field changes sign and reaches the coercive field, the bias fingerprints rearrange at the coercive field. This shows that the domain walls generate significant electron-phase shifts, at least on the order of π. But since the change in the bias fingerprint is discontinuous, we do not know yet how much phase is affected by the domain wall.

5.3.1 Fluctuations in Resistance in Strong Field

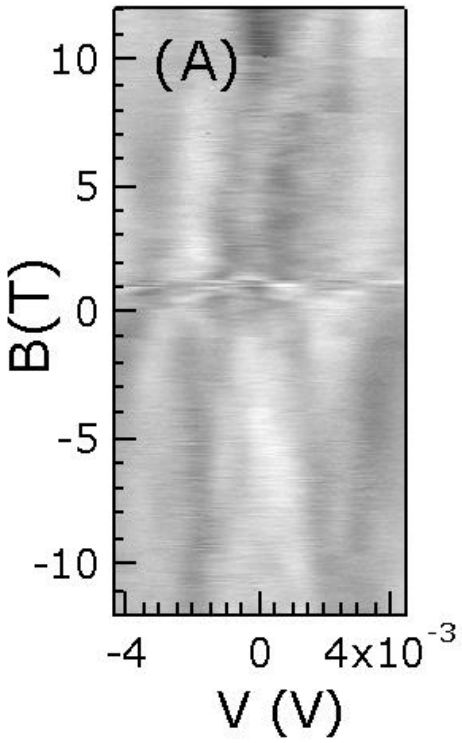

Figure 5.10: Fluctuations in differential resistance in strong in-plane field.

Before discussing the physical origin of the rearrangements in bias fingerprints, we analyze the strong field data in figures 5.10 and 5.11, 2 T $< |B| <$ 12 T. In this field range, we attribute the fluctuations to Aharonov-Bohm effect. Comparing figures 5.10 and 5.11 in this field range, we observe that bias fingerprints vary faster with the OP field. Alternatively, the characteristic field scale, which rearranges the bias fingerprint in strong field, is smaller in the OP direction. The correlation field B_C is the average spacing between the bright and

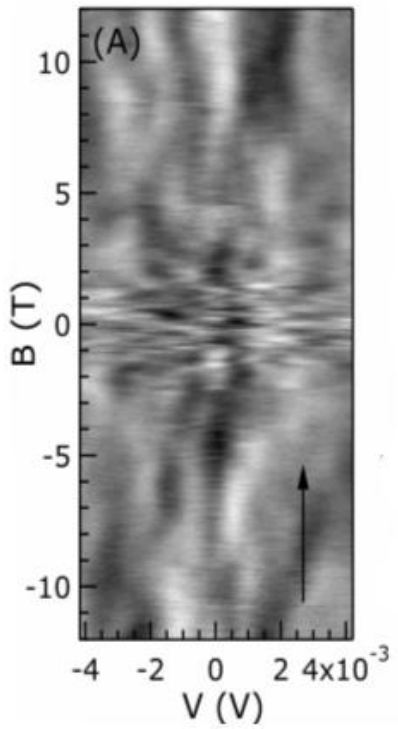

Figure 5.11: Fluctuations in differential resistance in strong out-of-plane field.

dark regions along B axes; $B_C \approx 4$ T and it is weakly dependent on V, confirming that the heating is not significant.

In a strong OP field, magnetization is saturated, and B_C is given by the field for a flux quantum over the phase-coherent area,

$$B_C = \Phi_0 / L_\phi^2 \tag{5.11}$$

where

$$\Phi_0 = h/e \tag{5.12}$$

is the flux quantum, and L_φ is the dephasing length. Then we find

$$L_\phi = \sqrt{\Phi_0 / B_C} \approx 30nm \tag{5.13}$$

Assuming a mean-free-path $l = 5$ nm and the Fermi velocity $v_F = 1.4 \times 10^6 m/s$, the electron dephasing time is

$$\tau_\phi = L_\phi^2 / (v_f l/3) = 0.4ps, \tag{5.14}$$

in agreement with τ_φ obtained before, within an order of magnitude. In the IP direction, B_C is larger, because the phase-coherent area perpendicular to the field is smaller,

$$B_C = \Phi_0 / t L_\phi \approx 12T \tag{5.15}$$

where t is the thickness of the Co film.

5.3.2 Bias Fingerprints rearrangements at Coercive Fields

Now we discuss the rearrangements in bias fingerprints at the coercive fields, figure 5.12 and 5.13). The internal field switches at the coercive fields. In Co, the internal field change is less than 3.6 T, much smaller than the IP field for a flux quantum (12 T). So the Aharonov-Bohm effect cannot be responsible for the rearrangements.

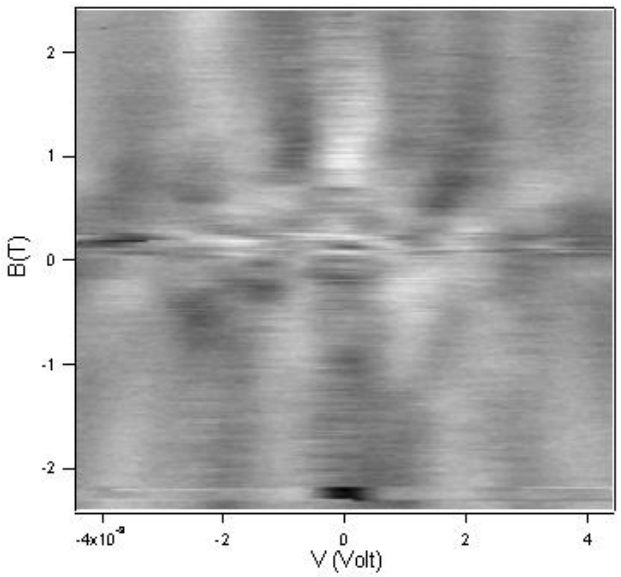

Figure 5.12: Fluctuations in differential resistance in weak in-plane field.

Figure 5.11 shows that the density of bright and dark regions increases when $|B| < 1.5$ T. Then we zoom in the weak field region in figure 5.13. There are about five bright and dark regions along B axes between 0 and 1.5 T. This shows that the magnetization rotation form IP to OP direction creates a phase shift along a typical phase-coherent electron trajectory of about 5π. Since the total field (internal field plus applied field) changes by less than 3.3 T in this applied field range and the OP field for a flux quantum is about 4 T , five resistance

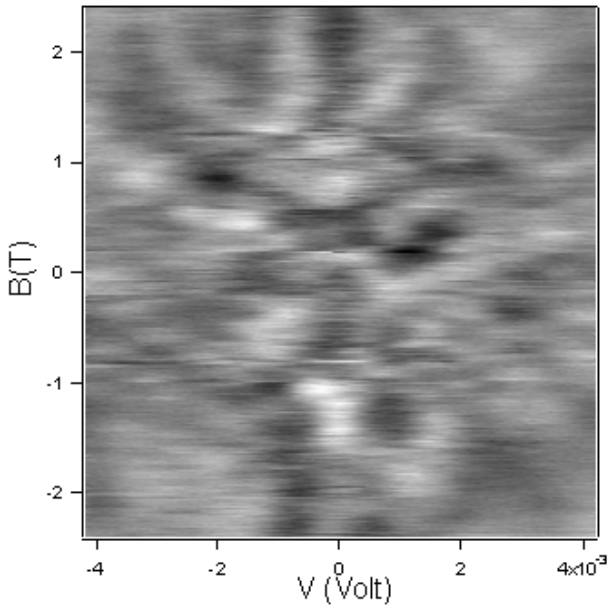

Figure 5.13: Fluctuations in differential resistance in weak out-of-plane field.

minima and maxima cannot originate from the Aharonov-Bohm effect. So the fingerprints rearrangement at coercive fields in both IP and OP field directions must originate from some other mechanisms.

We think it is the domain wall generate the 5π phase. Tatara et al. predicted an effect to arise from motion of the domain wall. But it is not likely in our experiment, because our nanomagnets are very small. We think that the phase shift could originate from a weak mistracking effect (see figure 5.14 when conduction electron spins lag behind the magnetic moments in the domain wall [30, 31, 61, 35]. The conduction electron spin tracks the local exchange field well when the angular rotational period around the exchange field is much smaller than the time of flight across the wall, which is equivalent to a large value of the tracking parameter

$$\xi = 2E_{ex}\delta_w/hv_F. \tag{5.16}$$

Here, E_{ex} is the exchange energy between conduction electron spins and the spins responsible for ferromagnetism and δ_w is the domain wall width in Co. Transport is adiabatic if $\xi >> 1$. After a conduction electron traverses the wall, the angle between the exchange field direction

and the conduction electron spin is

$$\theta \approx 1/\xi = 0.14. \tag{5.17}$$

So the electron transport through the domain wall is weakly unparallel. Using $E_{ex} = 1$ eV

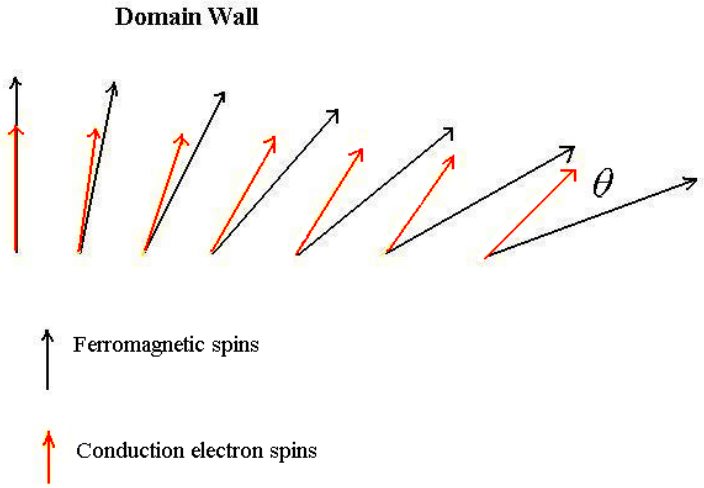

Figure 5.14: Mistracking effect: electron spins lag in orientation with respect to the moments inside the domain wall.

and $\delta_w = 15$ nm, one obtains [30]

$$\xi = \frac{2E_{ex}\delta_w}{h v_f} \approx 7.3 \tag{5.18}$$

After passing the domain wall and weakly unparallel transport, the angular deviation increases the effective potential energy of the conduction electron by

$$\Delta = E_{ex}[1 - Cos(\theta)] \approx E_{ex}/2\xi^2 = 9meV. \tag{5.19}$$

The increase in effective potential energy contributes to DWR [30, 31, 61, 35]. In mesoscopic transport, however, electrons interfere among trajectories with diffusion times shorter than τ_φ, which leads to a correction in sample resistance. The phase of the wave function is:

$$\varphi_i = \frac{eV}{2}t_i + \frac{1}{\hbar}\int_0^{\min(t_i,\tau_\varphi)} \left(\left(\vec{p} - e\vec{A}\right)^2 \Big/ 2m + U\left(\vec{r}\right) + \vec{J}_S\vec{S}\left(\vec{R}\right) \right) dt \tag{5.20}$$

where $\vec{S}(\vec{R})$ is 9 meV.Then the wave function attains a phase shift $\delta\varphi_i$ from this effective potential is:

$$\delta\varphi_i = \frac{1}{\hbar}\int_0^{\min(t_i,\tau_\varphi)} \Delta\left(\vec{J}_S\vec{S}\left(\vec{R}\right)\right)dt = \frac{\Delta\tau_\varphi}{\hbar} \approx 4.8\pi \tag{5.21}$$

So the bias fingerprints should rearrange about 5 times when they rotate in to the OP direction. The phase shift is reduced to zero when the magnetic moments become parallel with each other. In this case, $\theta = 0$, then $cos(\theta) = 1$, thus the increased effective potential energy of the conduction electron Δ is zero and consequently $\delta\varphi_i = 0$.

5.3.3 Short Coherence length and Dephasing time in Cobalt

The dephasing length we found in this experiment is $L_\varphi = 30$ nm, which is very short. In a separate experiment, we measured two Co nanowires of lengths 500 nm and 800 nm and width 100nm at T = 0.03 K. These nanowires displayed no conductance fluctuations, confirming that $L_\varphi << 500$ nm.

The dephasing process in ferromagnets is not well understood. In permalloy, experiments suggest that two level systems are important sources of dephasing [13]. Theoretically, domain walls were are found to reduce the dephasing length [2]. But, the dephasing time

$$\tau_\varphi = \hbar/eV_C \tag{5.22}$$

in our samples is independent of B; τ_φ in strong field , where the ferromagnet is in a single domain state, is approximately the same as τ_φ at $B = 0$ when domains are present. This demonstrates that the domain walls can not responsible for the short dephasing time τ_φ.

The phase of the wave function is extremely sensitive to the position or presence of domain walls, as indicated by the rearrangement of bias fingerprints in figure 5.9. The absence of domain wall contribution to dephasing suggests that the electron interaction with the wall must be elastic, since elastic collisions do not destroy quantum coherence. This situation is analogous to the sensitivity of conductance fluctuation with respect to changes in the impurity configurations [6, 8, 9]. In a thin film mesoscopic sample, motion of an impurity by the Fermi wavelength rearranges conductance fluctuations. Nevertheless, the impurities do not contribute to dephasing when electron scattering is elastic.

Kasai *et al.* found very short L_φ in Ni, $L_\varphi \approx 80$ nm [12]. Small L_φ is correlated with the large magnetocrystalline anisotropy in Ni; the dephasing length in NiFe permalloy, which has negligible magnetocrystalline anisotropy, is 500nm. since the magnetocrystalline anisotropy in Co is stronger than that in Ni, the dephasing length of 30nm in Co agrees with the trend that L_φ decreases with magnetocrystalline anisotropy [12].

In conclusion, we conduct the experiment to demonstrate mesoscopic resistance fluctuations induced by the magnetization-reversal process in a Co nanoparticle for the first time. The resistance fluctuations are explained by the spin mistracking effect in electron transport through domain walls. The dephasing length at low temperatures is only 30 nm, which is attributed to the large magnetocrystalline anisotropy in Co, in agreement with the trend established before, but not understood theoretically.

CHAPTER VI

EXPERIMENTS ON NIFE NANOPARTICLES

6.1 Introduction

This chapter describes a follow-up experiment to the Co nanoparticles experiment in the previous chapter. The phase shift of about 5π observed in our Co nanoparticles has been attributed to the domain wall. Then what will the phase shift be if there are no domain walls? To answer this question, we need single domain nanoparticles where domain walls are absent. The permalloy NiFe should be a good choice to make single domain nanoparticles because the domain wall width in NiFe films are much longer than in similar-sized Co films. A plot of NiFe domain wall width *vs* film thickness is shown in figure 6.1 [71], where we can see that the width of a 180° Neel wall in a 10-nm-thick NiFe film is between 150 nm and 200 nm. Thus, a NiFe nanoparticle with 200-nm diameter and 10-nm thickness can barely support a domain wall, i.e., the chance to get a single domain nanoparticle is greatly enhanced.

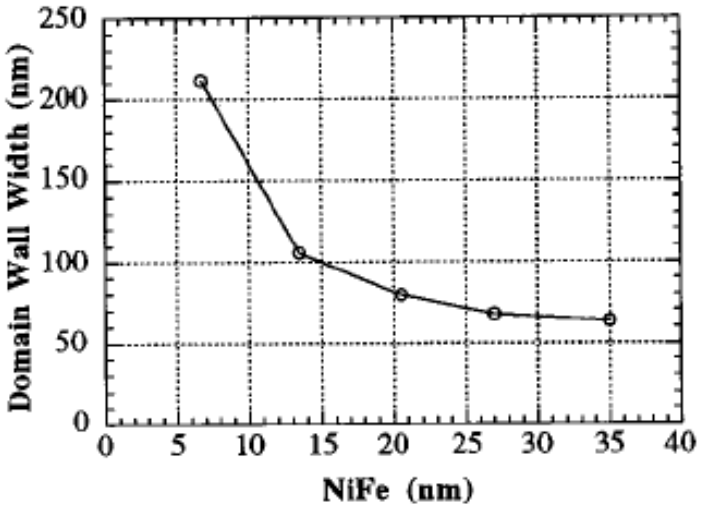

Figure 6.1: Plot of 180° NiFe domain wall width *vs* film thickness.[71]

Besides, in mesoscopic NiFe samples with similar dimensions to our Co samples, it should be easier to observe the conductance fluctuations. The reason is the permalloy NiFe has negligible magnetocrystalline anisotropy, thus it has a much longer phase coherence length L_ϕ. Kasai et al. found the phase coherence length in their NiFe nanorings as long as 500 nm [12], which is more than an order longer than the phase coherence length of about 30 nm found in our Co nanoparticle. Another advantage to use NiFe is this permalloy is much more stable to oxidation than cobalt, thus the exchange bias effect is reduced significantly. In this experiment, we use the NiFe permalloy composed of 80% Ni and 20% Fe.

6.2 Sample Fabrication

The NiFe nanomagnet samples are made by electron beam lithography and high vacuum shadow evaporation and they look very similar to the Co nanomagnet sample. Although the NiFe samples have the same geometry as the Co nanomagnet samples in the previous chapter, there are some subtle modifications we make during the shadow evaporation step. We add two permanent magnets on the rotary stage with their magnetic poles properly aligned as shown in figure 6.2. These two magnets help align the NiFe magnetocrystal polarization during deposition to further reduce the magnetocrystalline anisotropy, thereby raise the chance to get a single domain nanoparticle. In addition, we deposit a protective layer of gold (Au) *in situ.*, which is not present in the Co nanomagnets. This gold cap layer over the NiFe film can protect it from surface oxidation, thus remove the exchange bias effect we have had in Co nanomagnets.

The electron beam lithography procedure in making NiFe nanoparticles is identical to making Co nanoparticles. So here we only describe the thermal evaporation procedures. After the patterned sample is developed, we attach it onto the evaporation stage with the alignment shown in figure 6.2, and load the stage into the high vacuum evaporation chamber. Then we pump down the chamber until the pressure reaches the base pressure of 10^{-7} *torr* before we can start the evaporation. First, we deposit NiFe permalloy vertically at the rate of 0.2 nm/s, the deposition is stopped when the film thickness reaches 10 nm. Then we vertically deposit a Au layer of 2-nm thickness at the rate of 0.5 nm/s. Then we

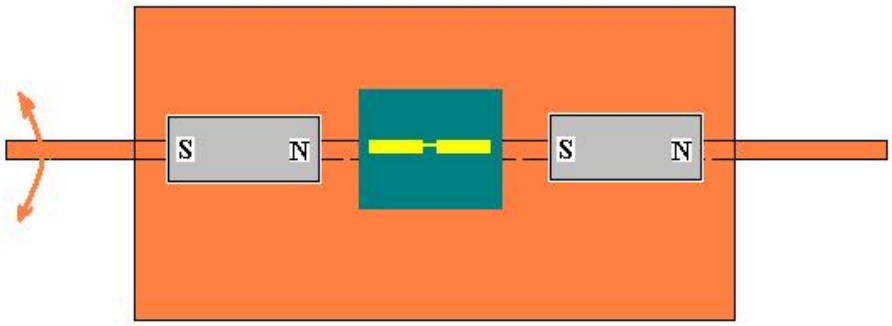

Figure 6.2: Top view of the stage. Two permanent magnets are added as shown to align the NiFe magnetocrystal polarization during deposition.

deposit a Cu layer of 50-nm thickness at the rate of 0.5 nm/s using 30° shadow evaporation. All of the three steps are done in series without breaking the vacuum, and the interfaces between layers are free from adsorbates because the transition times between steps are less than 10 seconds. The NiFe nanoparticle is isolated from other ferromagnetic area in a vicinity of 1.5 μm to remove the influence of stray magnetic field from other ferromagnetic parts of the device. A schematic diagram of the three deposition steps is shown in figure 6.3. After lift off, we obtain our NiFe nanomagnet samples. Then the sample is mounted with the four probe structure and transferred to the dilution fridge for measurement. The differential resistance is measured in a four-probe configuration using a lock-in amplifier. The measurement circuit setup is the same as figure 4.2.

6.3 Experimental Data

6.3.1 In-plane Data

First, we place the sample in the dilution fridge such that the magnetic field is perpendicular to the NiFe nanoparticle easy axis, and lying in the NiFe film plane (in-plane perpendicular field). The easy axis is along the electric current direction.

Differential resistance $r = dV/dI$ is recorded by a lock-in amplifier. At the base temperature $T = 45$ mK, we take a typical magneto-resistance trace (shown in figure 6.4)

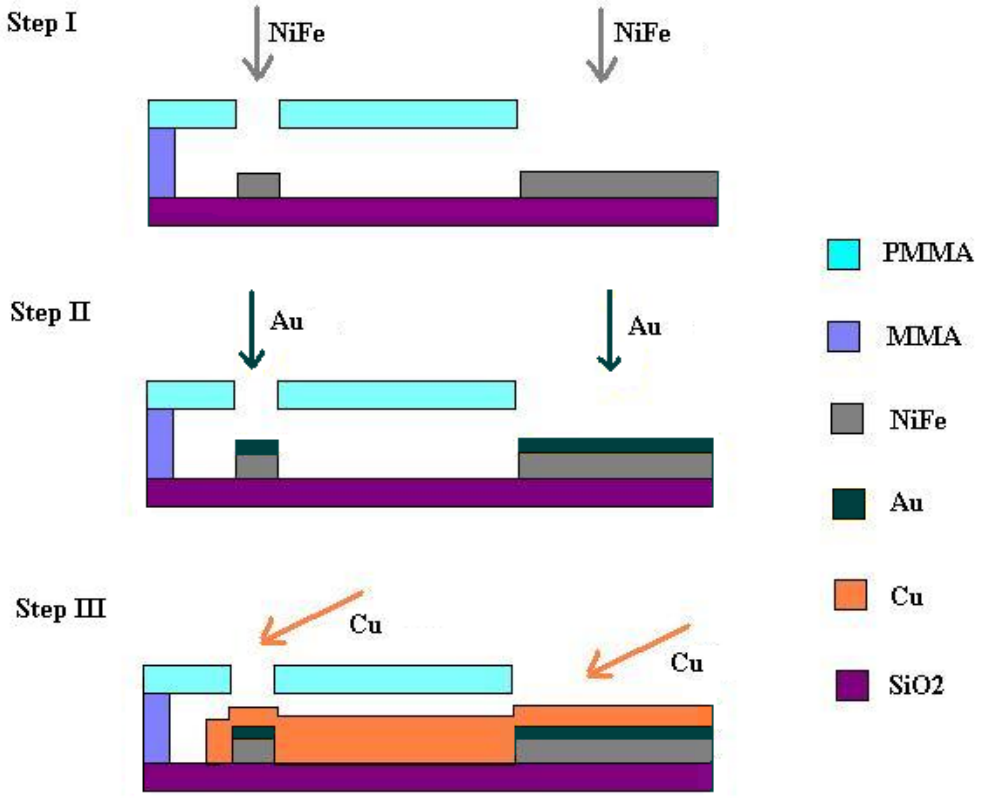

Figure 6.3: Deposition steps of NiFe nanoparticles. I: Vertically deposit a NiFe layer of $10-nm$ thickness. II: Vertically deposit a Au layer of $2-nm$ thickness. III: Deposit a Cu layer of $50-nm$ thickness with 30 degree shadow evaporation.

with zero DC bias first. The applied AC current is

$$I_{AC} = icos(2\pi ft); \tag{6.1}$$

where i = *0.3* μA, and f =231 Hz. The magnetic field B is from -0.1 T to 0.1 T and then back to -0.1 T at a constant rate of 0.2 mT.

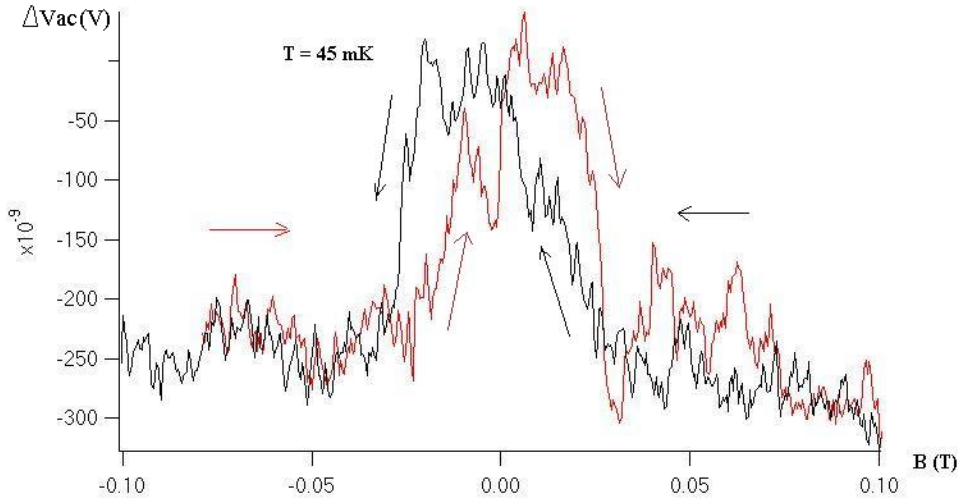

Figure 6.4: Magnetoresistance at $T = 45$ mK. The differential resistance is taken using the offset mode of the lock-in amplifier, thus the background resistance has been subtracted. The in-plane magnetic field is scanning between -0.1 T and 0.1 T.

The magneto-resistance curve exhibits a clear hysteresis. It has a broadened peak in each field direction. As the magnetic field is scanning between -0.1 T and 0.1 T many times (see figure 6.5), we can see that the peaks are reproducible. ic . The coercive fields in each field direction are symmetric , $B_C = \pm$ 250 mT. There is only one sharp transition of resistance in each field direction. The resistance change can be explained by AMR. As the magnetization rotates from perpendicular to current at strong fields (tails in MR curve) to parallel to current at weak fields (peaks in MR curve), the angle between magnetization and current reduced, thus the resistance increases.

To study the resistance fluctuations in our NiFe samples, we employ the differential resistance versus bias DC voltage (V) and IP magnetic field (B) scan, *r (V,B)*. After we subtract the average resistance versus field $r_0(B)$ and the average resistance versus bias voltage $r_0(V)$ from *r (V,B)* like what we did in the Co experiment, we couldn't see obvious

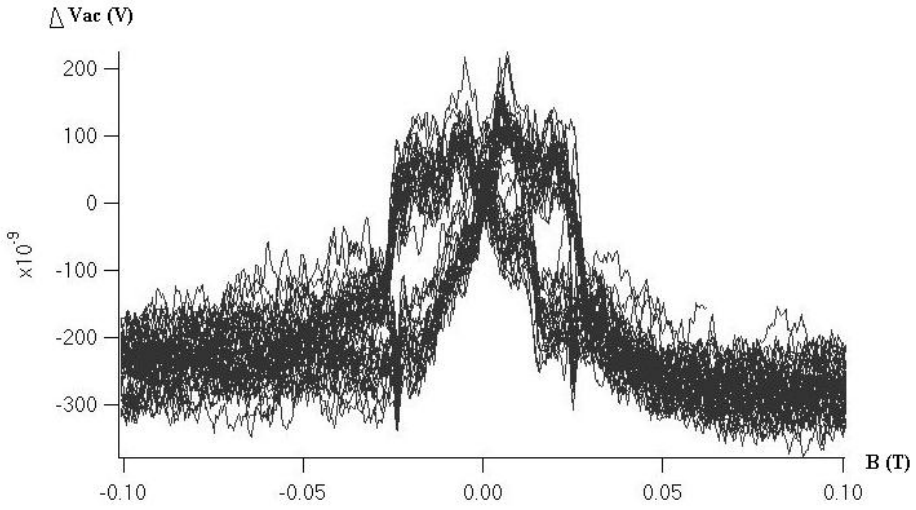

Figure 6.5: Magneto-resistance at 45 mK. The differential resistance is taken using the offset mode of the lock-in amplifier. The in-plane magnetic field is scanning between -0.1 T and 0.1 T many times to show the reproducibility and symmetry.

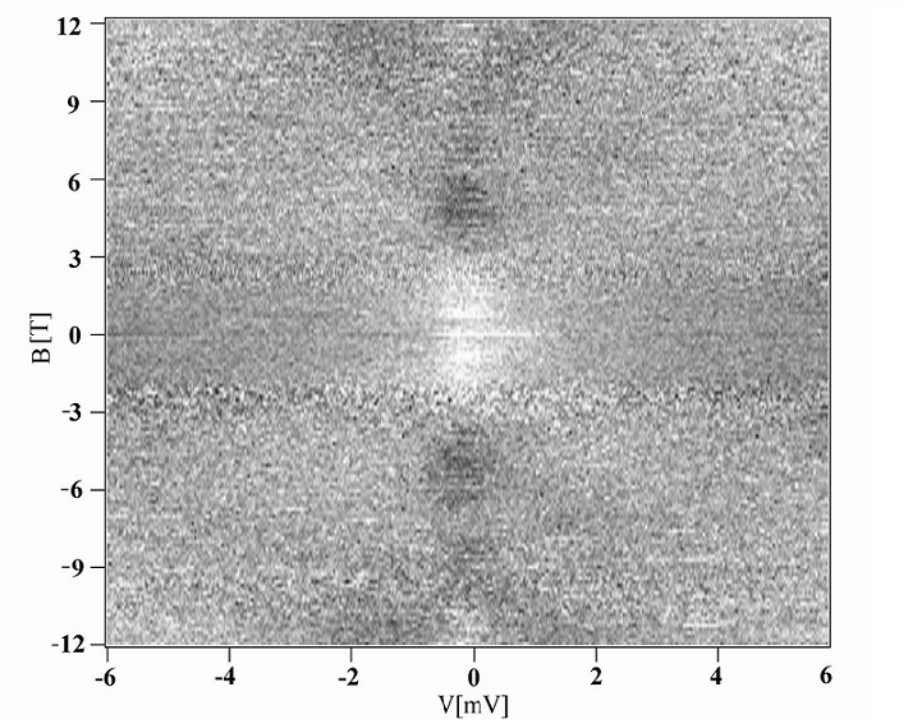

Figure 6.6: Differential resistance r versus bias voltage V and in-plane magnetic field B at 45 mK. Data is taken by quickly sweeping the bias voltage and slowly sweeping the magnetic field. Brighter pixels represent higher resistances.

fluctuations in resistance.

6.3.2 Out-of-plane Data

Not observing conductance fluctuations could be due to the correlation field larger than 12 T . Then the fluctuations are more likely to be observed in the out-of-plane field, where the correlation field is lower because the phase coherent area perpendicular to the field is larger than in the in-plane field. In the out-of-plane field , the correlation field is

$$B_{C\perp} = \frac{\Phi_0}{L_\phi^2} \tag{6.2}$$

while

$$B_{C//} = \frac{\Phi_0}{tL_\phi} \tag{6.3}$$

for in-plane field, where $t = 10$ nm is the thickness of our sample. Since t is much smaller than 500 nm [12], the expected phase coherent length in NiFe, $B_{C\perp}$ is supposed to be much smaller than $B_{C//}$.

We take the *r(V,B)* scan at base temperature $T = 45$ mK in the out-of-plane magnetic field. The sample resistance versus bias voltage and magnetic field is shown in figure 6.7. The data turns out to be unexpectedly different. In the weak OP field, The maxima in the V_{ac} versus V_{dc} curve due to EE effect became minima (refer to the dark region in figure 6.7). The resistance fluctuations are not shown, either.

We then take a series of V_{ac} versus V_{dc} data at different temperatures in both zero field and 0.1 T field. Figure 6.8 to figure 6.11 show four pairs of curves taken at 750 mK, 1.2 K, 1.8 K and 3 K respectively. These traces exhibit themselves strong temperature and field dependence.

The magnetoresistance curve taken at T = 750 mK with out-of plane field sweeping between -0.1 T and 0.1 T is shown in figure 6.12. It is really unfamiliar and too complicated to be understood. It is symmetric about zero field and has a flat minima. There are four separate transitions in each field direction. Some intermediate state seems to be present. This cannot be explained by AMR in ferromagnetic materials, because the resistance in the low field range is supposed to be larger than in strong field due to the decreasing angle

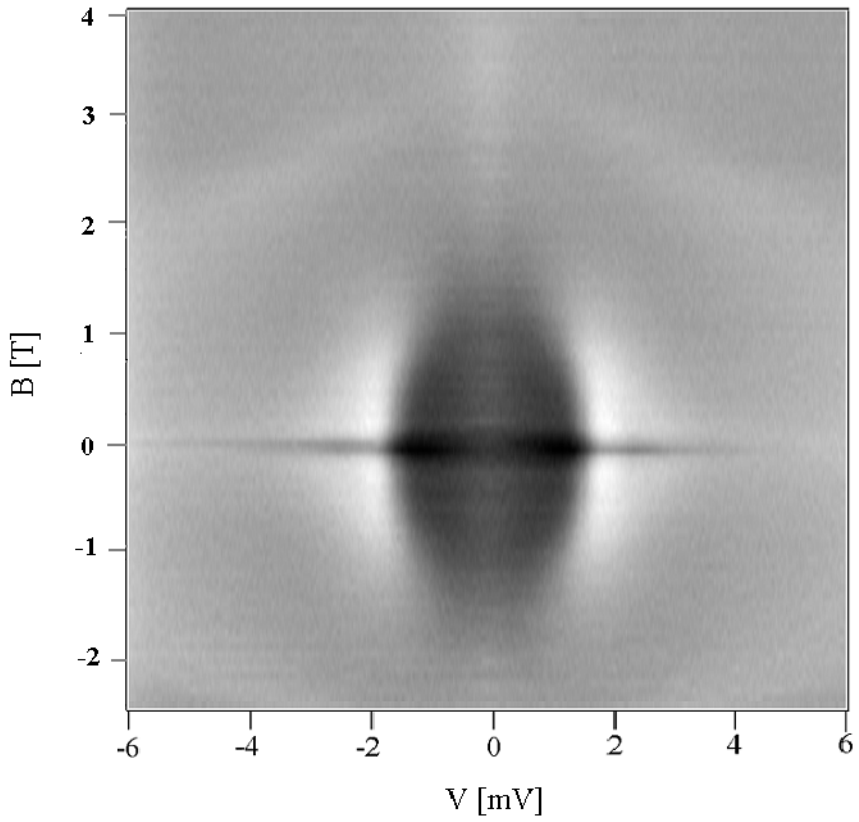

Figure 6.7: Differential resistance r versus bias voltage V and out-of-plane magnetic field B at $T = 45$ mK.

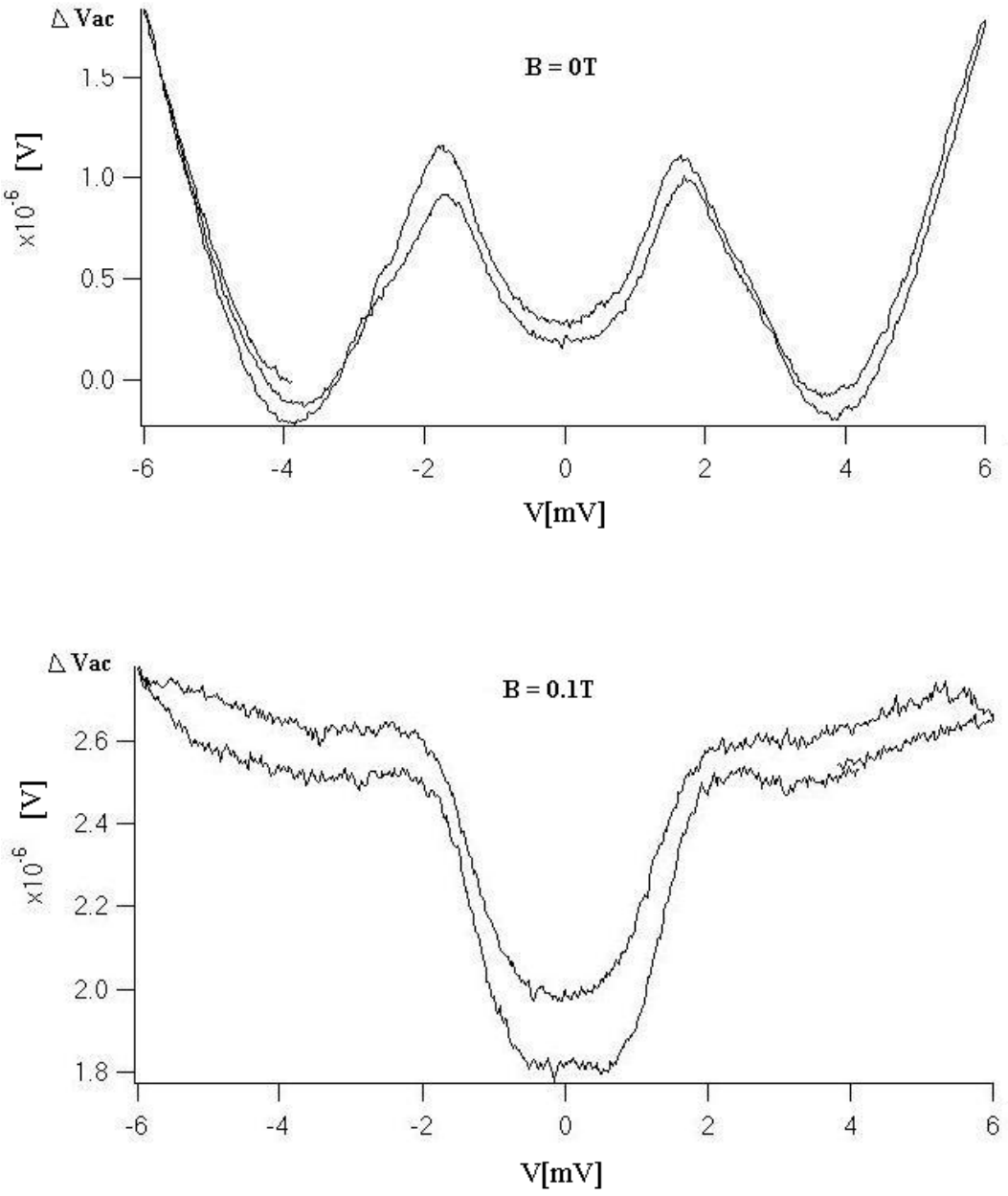

Figure 6.8: V_{ac} versus V_{dc} at $T = 0.75$ K for zero field and 0.1 T out-of-plane field.

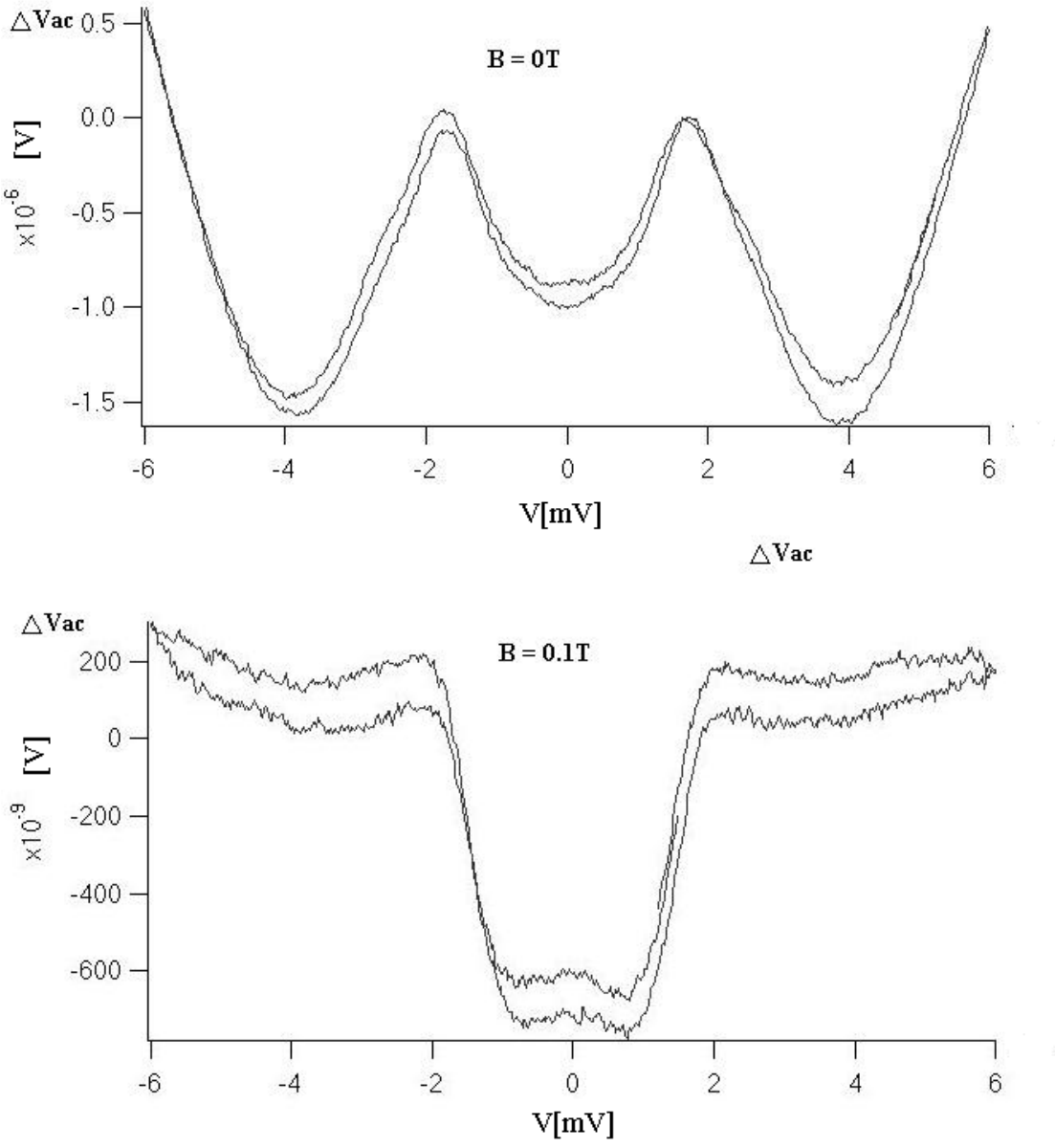

Figure 6.9: V_{ac} versus V_{dc} at $T = 1.2$ K for zero field and 0.1 T out-of -plane field.

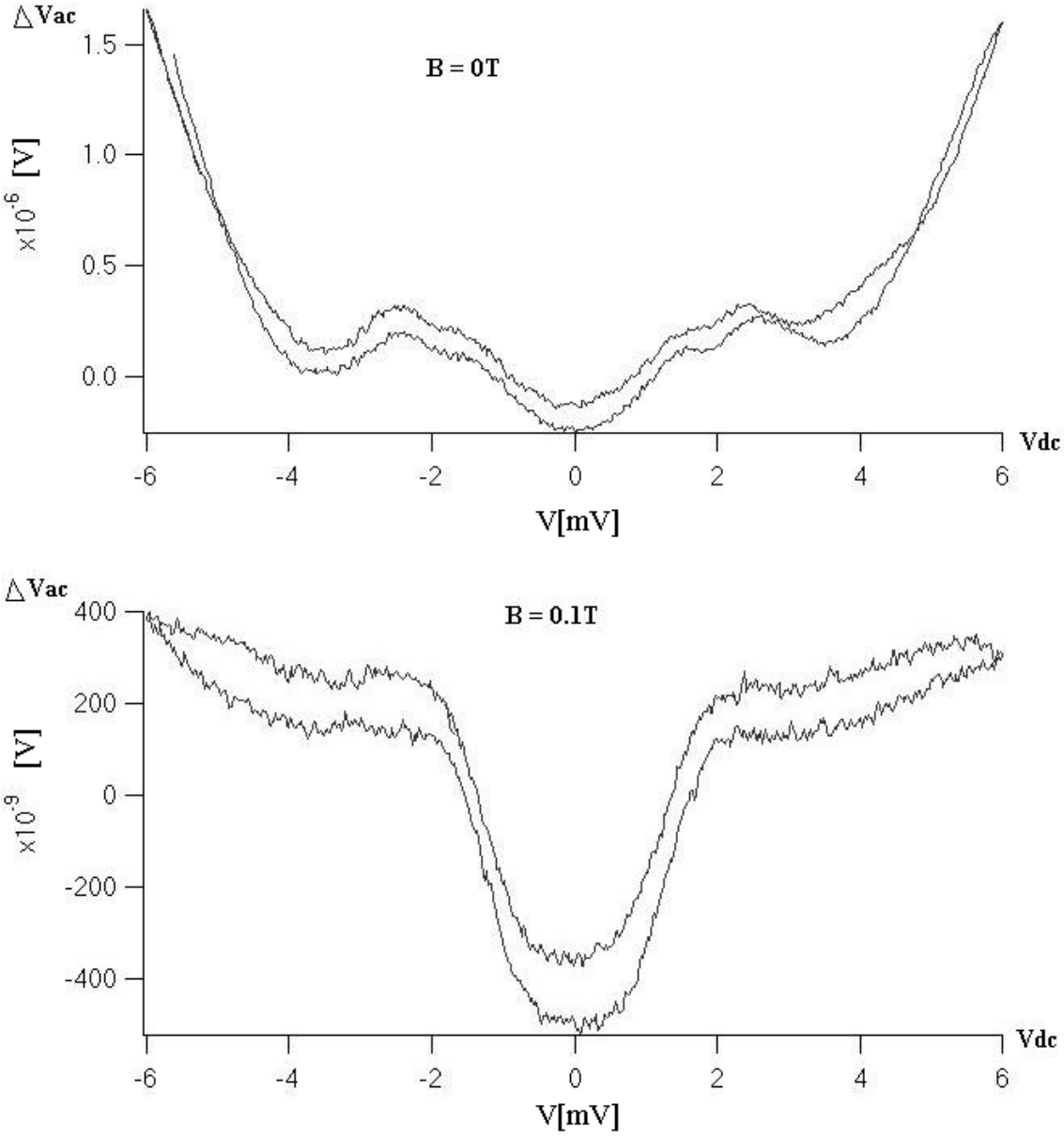

Figure 6.10: V_{ac} versus V_{dc} at $T = 1.8$ K for zero field and 0.1 T out-of-plane field.

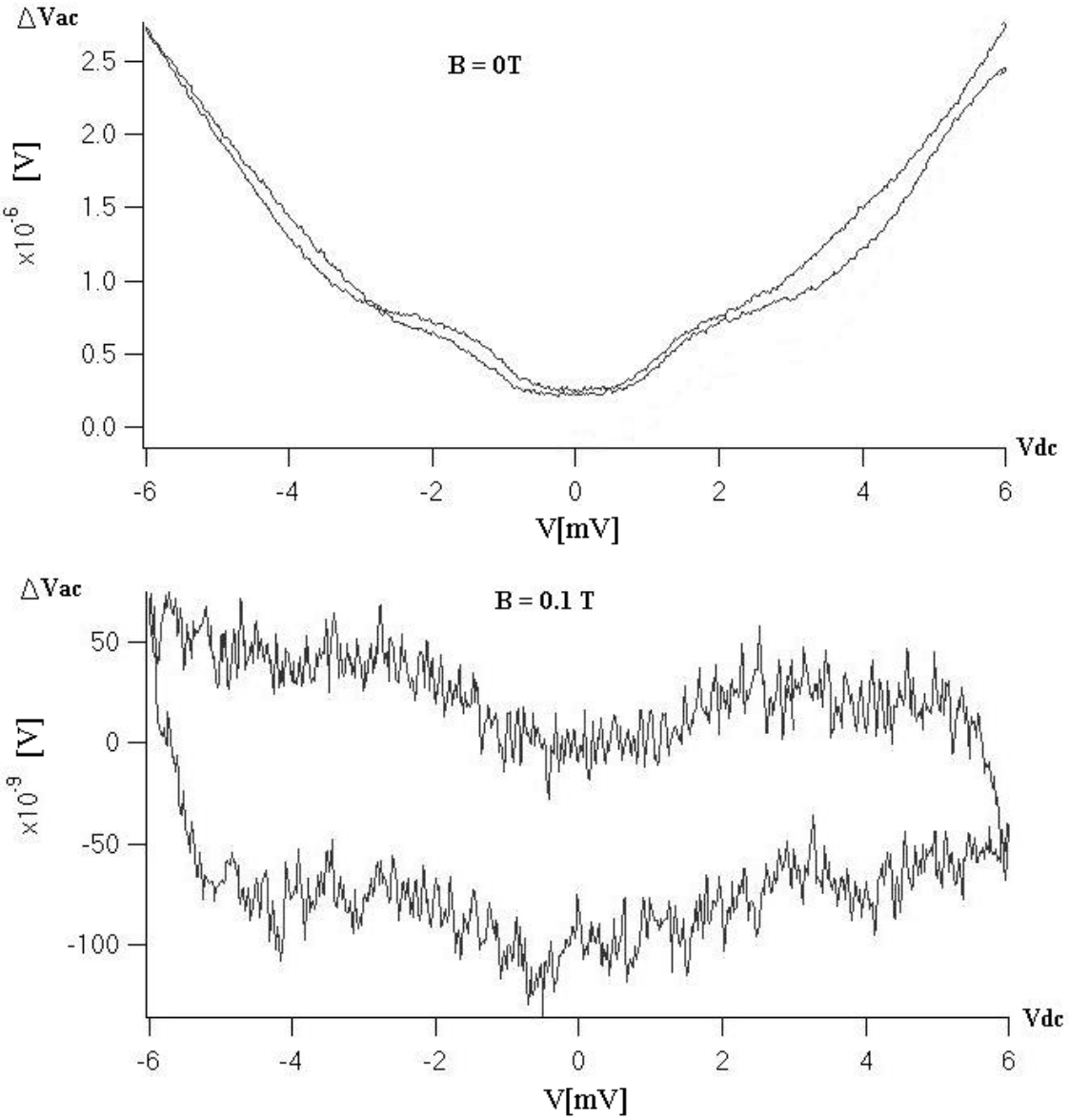

Figure 6.11: V_{ac} versus V_{dc} at $T = 3$ K for zero field and 0.1 T out-of-plane field.

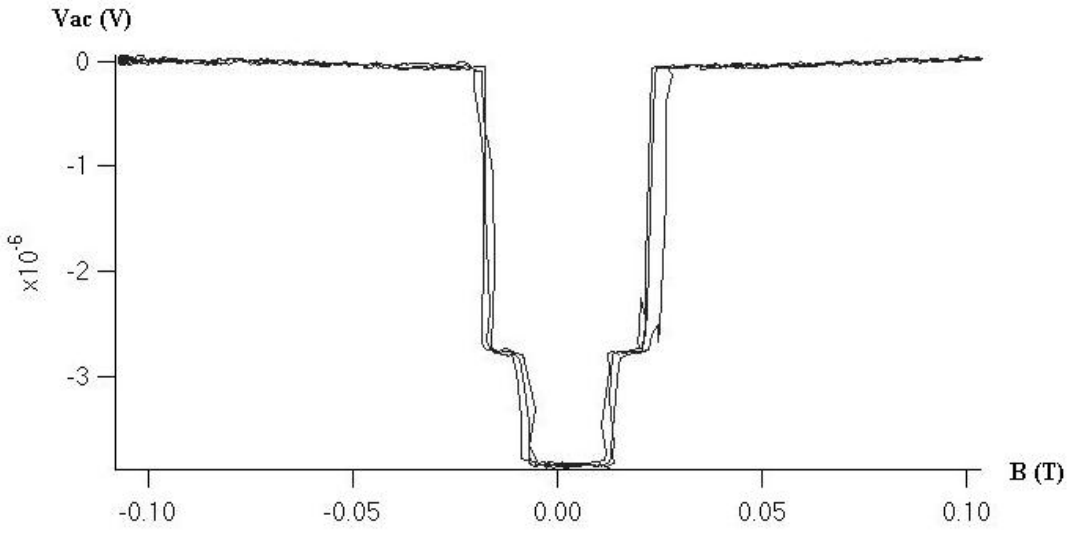

Figure 6.12: Magnetoresistance at T = 0.75 K. Out-of plane magnetic field is sweeping between -0.1 T and 0.1 T.

between magnetization and current as field goes to zero. Since we have a Au cap layer covering the NiFe film, it maybe due to some interactions between the normal metal gold layer and the ferromagnetic NiFe layer.

6.4 Conclusions

In our mesoscopic Au capped NiFe nanoparticles, magnetoresistance fluctuations are not clearly shown in both in-plane and out-of-plane magnetic fields. The dephasing at the Au/NiFe interface could be a possible cause for it. Innovative phenomena in OP field are observed but hard to be explained at this time. In out-of -plane field, the V_{ac} versus V_{dc} feature is very sensitive to both temperature and applied magnetic field. A new magnetoresistance feature is also observed in out-of-plane field at base temperature. We think these novel phenomena are somehow related to the interaction between NiFe and Au, since explaining the phenomena by properties any of them separately are not applicable.

CHAPTER VII

CONCLUSION AND FUTURE WORKS

In this thesis, we present measurements on mesoscopic ferromagnetic samples. In Co nanomagnets, mesoscopic resistance fluctuations are measured. We study how the fluctuations respond to magnetization-reversal process. Bias fingerprints rearrange when domains are nucleated or annihilated. At coercive fields, a phase shift of around 5π is observed and attributed to the domain wall scattering by the mistracking effect. From the correlation voltage, we found the dephasing time in Co is 1.3 *ps*. From the correlation field, we found the coherence length in Co is about 30 *nm* and the dephasing time is 0.4 *ps*, which is in agreement with 1.3 *ps* found from correlation voltage in the same order. We think it is the high magnetocrystalline anisotropy of Co that leads to the short dephasing time about 1 *ps*. The absence of domain wall contribution to depahsing suggests that the electron interaction with the domain wall must be elastic.

In the Au capped NiFe nanomagnets, novel phenomena have been observed for the first time. The fluctuations in magnetoresistance is suppressed. These could be due to dephasing at the Au/NiFe interface and the interaction between NiFe and Au. Further experiments can be conducted to systematically examine how the thickness of the Au cap layer will affect the magnetoresistance.

APPENDIX A

LIST OF SYMBOLS

$\overset{o}{A}$	Angstrom, Unit of Length (1 $\overset{o}{A}$ =$10^{-10}m$)
PMMA	Polymethyl Methacrylate
MMA	Methacrylic Acid , Copolymer
SEM	Scanning Electron Microscope
MR	Magneto-resistance
AMR	Anisotropic Magneto-resistance
DWR	Domain wall resistance
IP	In-plane
OP	Out-of-plane
CF	Conductance Fluctuations
Co	Cobalt
Ω	Ohm, Unit of resistance
Φ_0	Flux Quantum
L_ϕ	Phase Coherence Length
τ_ϕ	Dephasing Time
δ_w	Domain Wall Width
ξ	Tracking Parameter
e	Elementary Charge ($1.602 \times 10^{-19} Coulombs$)
eV	Electron Volt, Unit of Energy (1eV = 1.602×10^{-19}joules)
T	Tesla, Unit of Magnetic Field
torr	Unit of Pressure (1 *torr* = 133.32 pascals)

nm	Nanometer, Unit of Length ($1\ nm = 10^{-9}\ m$)
μm	Micron, Unit of Length ($1\ \mu m = 10^{-6}\ m$)
B_C	Correlation Field
V_C	Correlation Voltage
v_f	Fermi Velocity
h	Planck Constant ($6.62 \times 10^{-34} J \cdot s$)
$\hbar$	Dirac Constant ($\hbar \equiv h/2\pi$)
EE	Electron-electron Interaction Enhancement
AB	Aharonov-Bohm
E_{ex}	Exchange Energy Between Conduction Electron Spins and Ferromagnet Spins
l	Mean Free Path
K	Kelvin, Unit of Temperature
t	Sample Thickness
R_s	Sheet Resistance
ps	Picosecond, Unit of Time ($1\ ps = 10^{-12}\ second$)
π	Irrational Number ($\pi = 3.1415926...$)
B	Magnetic Field
T	Temperature
mT	Milli-tesla, Unit of Magnetic Field (1 mT = 10^{-3} teslas)
EBL	Electron Beam Lithography
WLE	Weak Localization Effect
QC	Quantum Coherence
UCF	Universal Conductance Fluctuations
T_C	Curie Temperature
λ	Wave Length
n	Refraction Index
rpm	Revolution per Minute, Unit of Angular Speed
IPA	Isopropanol

MIBK	Methy Iso-butylketone
NPGS	Nanometer Pattern Generating System
PVD	Physical Vapor Deposition
CoO	Cobalt Oxide
Cu	Copper
Au	Gold
IVC	Inner Vacuum Chamber

REFERENCES

[1] D. Loss, H. Schoeller, and P. Goldbart, *Phys. Rev. B* **48**, 15218 (1993).

[2] G. Tatara and H. Fukuyama, *Phys. Rev. Lett.* **78**, 3773 (1997).

[3] S. Adam, M. Kindermann, and P. Brouwer, *cond-mat/0512287* .

[4] T. Mcguire and R. Potter, *IEEE Tran. Magn.* **11**, 1018 (1975).

[5] A. Kent, J. Yu, U. Rudiger, and S. Parkin, *J. Phys: Condens. Matter* **13**, R461 (2001).

[6] S. Washburn and R. Webb, *Rep. Prog. Phys.* **55**, 1311 (1992).

[7] C. Wu, W. Jian, and J. Lin, "Phonon-induced electron-electron interaction in disordered superconductors," *Phys. Rev. B* **52**, 15479 (1995).

[8] P. Lee and T. Ramakrishnan, *Rev. Mod. Phys.* **57**, 287 (1985).

[9] B. Altshuler and B. Spivak, "Pisma Zh. Eksp. Teor. Fiz. 42, 363," *JETP Lett.* **42**, 447 (1985).

[10] K. Hong and N. Giordano, *Phys. Rev. B* **51**, 9855 (1995).

[11] J. Aumentado and V. Chandrasekhar, *Physica(Amsterdam)* **284-288B**, 1742 (2000).

[12] S. Kasai, E. Saitoh, and H. Miyajima, *J. Appl. Phys.* **93**, 8427 (2003).

[13] S. Kee, A. Trionfi, and D. Natelson, *Phys. Rev. B* **70**, 212407 (2004).

[14] R. Potter and T. McGuire, "MAG-11," *IEEE Trans. Magn.* , 1018 (1975).

[15] J. Smit, *Physica* **XVI**, 612 (1951).

[16] S. Blundell, *Magnetism in Condensed Matter* (Oxford Master Series in Condensed Matter Physics, 2001).

[17] P. Chaikin and T. Lubensky, *Principles of Condensed Matter Physics* (, 1997).

[18] J. Ziman, *Principles of the Theory of Solids* (Cambridge: Cambridge University Press, 1986).

[19] A. Stone and A. Szafer, *IBM J. Res. Develop.* **32**, 384 (1988).

[20] D. Fisher and P. Lee, *Phys. Rev. B* **23**, 6851 (1981).

[21] N. Mott, "Proc. Royal Soc.," *London 153A* , 699 (1936).

[22] C. Kittel, *Introduction to Solid State Physics* (1986).

[23] J. P. Jan, *Solid State Physics* **5** (1957).

[24] J. Checkelsky, *Anisotropic Magnetoresistance of FexCo1-xS2* (Harvey Mudd College, 2004).

[25] A. Perrier, "Acta 3," *Helv. Phys.* , 400 (1930).

[26] W. Thomson, *Proc. Roy. Soc.* **8**, 546 (1857).

[27] R. Potter, *Phys. Rev. B* , 4626 (1974).

[28] G. Taylor, A. Isin, and R. Coleman, *Phys. Rev.* **165**, 621 (1968).

[29] G. Cabrera and L. Falicov, *Phys. Status Solidi* **61**, 539 (1974).

[30] J. Gregg, *et al. Phys. Rev. Lett.* **77**, 1580 (1996).

[31] M. Viret, *et al. Phys. Rev. B* **53**, 8464 (1996).

[32] M. Viret, *et al. Phys. Rev. Lett.* **85**, 3962 (2000).

[33] D. Ravelosona, *et al. Phys. Rev. B* **59**, 4322 (1999).

[34] U. Ruediger, J. Zhang, A. Kent, and S. Parkin, *Phys. Rev. Lett. 80* , 5639 (1998).

[35] P. Levy and S. Zhang, *Phys. Rev. Lett.* **79**, 5110 (1997).

[36] G. Tatara, "Phys. Soc. Jpn.," **69**, 2969 (2000).

[37] L. Berger, *J. Appl. Phys.* **49**, 2156 (1978).

[38] S. Datta, *Electronic Transport in Mesoscopic Systems* (Cambridge University Press, Cambridge, England, 2002).

[39] Y. Aharonov and D. Bohm, *Phys. Rev.* **115**, 485 (1959).

[40] G. Bergmann, *Phys. Rep.* **1**, 107 (1984).

[41] D. Sharvin and Y. Sharvin, *JEPT Lett.* **34**, 272 (1981).

[42] C. Umbach, S. Washburn, R. Laibowitz, and R. Webb, *Phys. Rev. B* **30**, 4048 (1984).

[43] S. Washburn, C. Umbach, R. Laibowitz, and R. Webb, *Phys. Rev. B* **32**, 4789 (1985).

[44] A. D. Stone, *Phys. Rev. Lett.* **54**, 2692 (1985).

[45] B. Al'shuler, *JEPT Lett. No.12* **54**, 2692 (1985).

[46] R. Landauer, *Philosophical Mag. No.172* **21**, 6851 (1970).

[47] M. S. Gupta, *IEEE TRANSACTIONS ON ELECTRON DEVICES* **41, NO. 11.** (1994).

[48] D. Thouless, *Phs. Rev. Lett.* **39**, 116 (1977).

[49] P. Lee, A. Stone, and H. Fukuyama, *Phys. Rev. B* **35**, 1039 (1987).

[50] P. Maldague, *Phys. Rev. B* **23**, 1719 (1981).

[51] Y. Imry, *Europhysics Lett.* **1**, 249 (1986).

[52] D. Biswas, A. Meikap, S. Chattopadhyay, S. Chatterjee, and J. Lin, *Physics Letter A* **328**, 380 (2004).

[53] B. Altshuler and D. Khmelnitskii, "JETP Lett.," **42**, 359 (1985).

[54] A. Millis and P. Lee, "Spin-orbit and paramagnon effects on magnetoresistance and tunneling," *Phys. Rev. B* **30**, 6170 (1984).

[55] B. Altshuler, A. Aronov, and A. Zuzin, "Spin relaxation and interaction effects in the disordered conductors," *Solid State Commun.* **44**, 137 (1982).

[56] A. White, R. Dynes, and J. Garno, "Correction to the two-dimensional density of states," *Phys. Rev. B* **31**, 1174 (1985).

[57] R. Dynes and J. Garno, "Metal-insulator transition in granular aluminum," *Phys. Rev. Lett. 46* , 137 (1981).

[58] P. Lee and A. Stone, *Phys. Rev. Lett.* **55**, 1622 (1985).

[59] B. Altshuler and A. Aronov, "Electron-Electron Interactions in Disordered Systems," *A.L. Efros and M. Pollak, Editors, Elsevier, Amsterdam* (1985).

[60] Y. Lyanda-Geller, I. Aleiner, and P.Goldbart, *Phys. Rev. Lett.* **81**, 3215 (1998).

[61] U. Ebels, *et al. Phys. Rev. Lett.* **84**, 983 (2000).

[62] S. Kim, *et al. IEEE trans. Magn.* **35**, 2862 (1999).

[63] R. Danneau, *et al. Phys. Rev. Lett.* **88**, 157201 (2002).

[64] D. Buntinx, *et al. Phys. Rev. Lett.* **94**, 017204 (2005).

[65] C. Yu, *et al. J. appl. Phys.* **94**, 8761 (2003).

[66] W. Meiklejohn and C. Bean, *Phys. Rev. Rev.* **102**, 1413 (1956).

[67] B. Hausmanns, T. Krome, and G. Dumpich, *J. Appl. Phys.* **93**, 8095 (2003).

[68] M. Brands, A. Carl, and G. Dumpich, *Europhys. Lett.* **68**, 268 (2004).

[69] B.Altshuler and A.Aronov, *Electron-Electron Interactrions in Disordered Systems* (Elseview, New York, 1985).

[70] K. Nagaev, *Phys. Lett. A* , 134 (1994).

[71] B. Y. Wong and D. E. Laughlin, *J. Appl. Phys.* **79**, 6455 (1996).

VITA

Xiya Liu was born in Nanjing, China, in October 1980. She received her Bachelor's Degree in Physics from Nanjing University, China, in 2002. Then she came to Atlanta, GA to pursue her graduate study and research at School of Physics, Georgia Institute of Technology . She joined Prof. Dragomir Davidovic's group, where she learned a series of experimental equipments and methods to study mesoscopic physics at low temperatures. Her research interest is focused on mesoscopic effects in ferromagnetic materials.